A Lizard-inspired Tube Inspector (LTI) Robot

DE-FE0031649

Final Report

Ehsan Dehghan-Niri (PI), Associate Professor, Intelligent Structures and Nondestructive Evaluation (ISNDE) Laboratory, New Mexico State University (niri@nmsu.edu ,nde@asu.edu)
Hamid Marvi (Co-PI), Associate Professor, Mechanical and Aerospace Engineering, Arizona State University (hmarvi@asu.edu)

Executive summary

This final report summarizes the research findings of the current project. This project is a collaboration between New Mexico State University (NMSU) as a lead (Recipient) and Arizona State University (ASU) as a Co-Recipient.

Tubular structures are common components of boilers and heat exchangers in power plants. Over time, these components may suffer corrosion, cracks, and stress-corrosion cracks in either the body or the welded connections. A single tube leakage can cause an outage of several weeks. Regular inspection is a key safety factor when ensuring that power plants are maintained in reliable, operational condition. This inspection, however, is challenging, time-consuming, and in many cases impossible due to accessibility issues and safety concerns. Recent developments in robotic-based inspection can offer a great solution. Hard-to-reach places can be inspected without overhauling the unit, saving time and cost. Although several robots have been designed and implemented successfully for inspecting power plant components, in particular tubular structures, their mobility and flexibility are limited. Most of these robots use wheels for mobility which reduces their maneuverability of these robots. Moreover, they usually use magnets to attach to tubes which will not work on tubes with non-ferromagnetic materials. These robots usually carry measurement tools for a particular non-destructive testing (NDT) method such as ultrasound testing (UT) that requires a couplant to perform a point-by-point (scanning) inspection of the tubular structure.

In this project, we developed a versatile lizard-inspired tube inspector (LTI) robot with embedded inspection sensing components for tube inspection which removes the need for point-by-point scanning of tube surface for crack and corrosion detection. Inspired by a “lizard”, the novelty of the current project is the integration of couplant-free ultrasound sensing and transmission, advanced data-driven defect detection and imaging, and friction-based mechanical mobility components in a single robot to eliminate a need for smooth surfaces and simple geometry for mobility and scanning. The LTI robot could replace the wheel-based approach with friction-based mobility to significantly increase the flexibility and maneuverability of the robot. The LTI robot can get into a power plant unit, such as a boiler, from a small area allowing it to access a component of interest for inspection (e.g., move on OD, curved and flat surfaces, non-ferromagnetic or ferromagnetic materials, and tubes with rough surfaces and complex geometries). Additionally, an advanced data-driven method using ultrasound data was pioneered to allow the robot to detect defects in the entire area between the robot’s multi-functional mobility system (grippers). Integrating a couplant-free ultrasound sensing in the robot’s grippers as well as using advanced data-driven methods allowed the LTI to detect defects in the entire cross-section of a tube using its grippers when stationary and when mobile.

Contents

List of figures

List of tables

1. Introduction

Power plants, which provide energy to surrounding cities, are important to everyday life and work and tubular structures are critical components of these plants. Throughout their life, these tubular structures experience extreme conditions or suffer from defects such as corrosion, cracks, and stress corrosion cracks. Therefore, it is necessary to regularly inspect them to ensure structural integrity. This is especially important because even small defects in the tubes can result in catastrophic failure and result in a power outage for weeks. However, frequent inspection of these structures is problematic due to various reasons. For example, most power plants that need to be inspected cannot be shut down as they are critical to the functioning of surrounding communities. In addition, safety risks, high temperatures, and limited access (hard-to-reach places) to these structures inhibit human inspection.

In this context, robotic inspection is a potential route to mitigate some of the safety restrictions faced by humans; furthermore, a robotic inspection would facilitate structural inspection in a timely and cost-effective manner. Tubular structures can be difficult to inspect because they often involve time-consuming testing methods for verifying their integrity. Two major types of robots being used for this purpose are in-pipe and out-pipe robots [1–4].

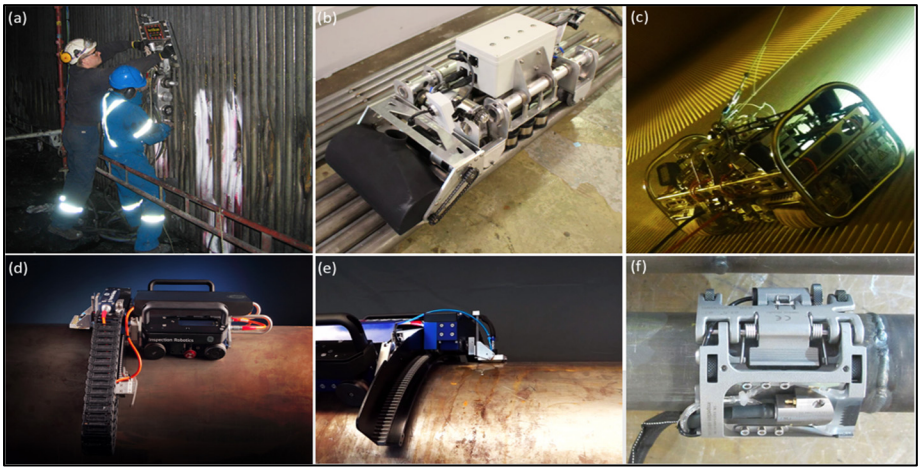

Figure 1. Tube inspection robots. (a) Vertiscan system, (b) ICM climbing robot, (c) boiler wall cleaning and inspection robot, (d) inspection robotics system, (e) FAST UT system, and (f) PALM scanner.

The first type, viz. in-pipe robots, focuses on inspecting the insides of pipes; the main limitation faced by these robots is that the power plant must be shut down during inspection, which affects plant productivity. Meanwhile, an out-pipe robot inspects tubular structures from the outside, thus allowing the plant to continue its operation. However, the main challenge facing the application of out-pipe robots is their limited mobility. For example, out-pipe robots must attach themselves to the structure using either friction or magnetic force and at the same time, maneuver around other obstacles [5]. Because an out-pipe robot does not require a plant to be shut down, assuming that the robot can traverse obstacles on the structure, this solution becomes the most cost-effective inspection method. Multiple wheel-based out-pipe inspection

robots have already been developed (see Figure 1) [4]. However, the disadvantage is that they can only be placed on a single pipe at a time. Once these robots are placed on a tube, workers will have to disassemble them before attaching them to another pipe. This exercise can be time-consuming and ineffective if a large tubular structure needs to be inspected. Therefore, we adopted a bioinspired approach and propose a robot with modular grippers with integrated non-contact ultrasound sensing elements to climb on vertical and horizontal surfaces using friction-based mobility. Thus, the objective of this study is to design and test a modular robotic gripper with an embedded couplant-free ultrasound system such as electromagnetic acoustic transducers (EMATs) as the main component of a versatile lizard-inspired tube inspector (LTI) robot (Figure 2).

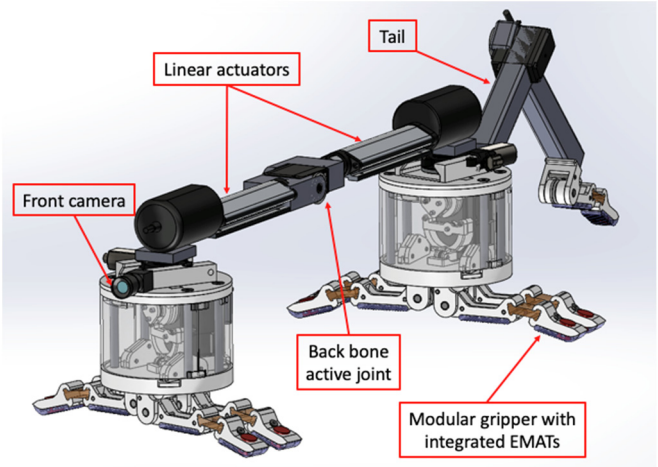

Figure 2. Conceptual design of the Lizard-inspired Tube Inspector (LTI) robot [4]

Ultrasound testing (UT) is the most effective non-destructive evaluation (NDE) method that can be integrated with robotic platforms for inspecting tubular components [6]. Robotic ultrasonic inspection is sensitive to both surface and subsurface flaws and different UT techniques may be used for different types of tests. For example, UT can be used to evaluate surface rust, thickness, and deficiencies in the structure being tested. Furthermore, the size of the equipment required for UT is relatively small which results in a light payload for the robot. Contact UT based on bulk or guided waves is time-consuming and requires prepared surfaces with adequate coupling for point-by-point scanning whereas non-contact ultrasound transmission mechanisms such as EMATs can effectively solve this problem. Two couplant-free mechanisms 1. EMATs and 2. Dry couplant are considered in this research for generation and reception of ultrasound Lamb waves around the pipe structures. In the first section, the nondestructive and sensing aspects of the project will be explained and in the following section, the robotic parts of the project will be covered.

2. Nondestructive evaluation and sensing

2.1. Couplant-free ultrasound generation

2.1.1. Electromagnetic acoustic transducer (EMAT)

Electromagnetic acoustic transducer (EMAT) is a transducer for non-contact acoustic wave generation and reception in conducting materials. EMATs are a promising well-known ultrasonic testing technique used in NDT of electrically conductive materials. The signal-to-noise ratio (SNR) in EMAT systems is inherently feeble. However, high amplification, filtering techniques, and narrow-band excitation can be useful to strengthen the SNR. Despite some of their limitations, including low efficiency, lift-off sensitivity, limited frequency range, etc., they have the big advantage of performing ultrasonic testing without any couplants. It permits easier deployment of probes, which is a remarkable privilege for automated inspections. This technique also facilitates the rapid scanning of components with complex geometries and unsmooth surfaces which was already mentioned as the main goal in LTI design. Traditional EMATs consist of a coil and a magnet and are used to generate ultrasonic waves in metallic samples that are under test. The coil is excited by an alternating electric current in presence of a uniform magnetic field near the surface of an electrically conductive or ferromagnetic material. This alternating Lorentz force plays the main role in transmitting waves as a source to produce oscillating stress waves. Depending on the design and orientation of the coils and magnets, different wave modes could be generated in EMAT applications. In other words, the orientation, size, and shape of the coil and the magnet configuration determine the type of ultrasonic waves and modes for different inspection purposes. In the following subsection, more details about the characteristics of EMATs used in LTI robot are provided.

In the LTI robot, Lamb waves are generated and received by integrated EMATs to eliminate point-by-point cross-section inspection of a tubular component. The main idea in the application of the Lamb waves in the LTI robot is that as the robot climbs, the network of eight EMATs in its two grippers can communicate and image the entire cross-section of the part of tubular component between the two grippers. As a type of guided ultrasound wave, Lamb waves can propagate in plate-like structures. For tubular structures with a small wall thickness-to- diameter-ratio, the circumferential waves in the tube wall can be considered similar to Lamb waves, by replacing the cylindrical structure with an equivalent unwrapped plate [7][8]. Lamb waves have unique properties that enable sophisticated inspection schemes. These waves, in general, can propagate long distances and are more sensitive to defects than traditional bulk ultrasound waves. The capability of Lamb waves to inspect the whole cross-section of a plate from a long distance makes them a practical choice in real-time monitoring and inspection of plate-like structures.

Lamb waves are inherently multi-mode and dispersive. Before investigating the detection and interaction of lamb wave modes with defects in pipes, it is necessary to represent their theoretical dispersion curves to select an effective mode. These curves are obtained from the governing differential equations and are a function of material properties and sample thickness [9]. Table 1 summarizes the properties used for determining the dispersion curvatures. The spiral coil (pancake coil) is used to generate omnidirectional Lamb waves to propagate in helical paths and cover the entire cross-section of the tube between the two grippers. A permanent Magnet (PM) generates the static magnetic field, whereas the spiral coil that the high-frequency

excitation current flows into, generates the dynamic magnetic field and then induces the eddy current in the skin depth of the specimens. The magnetic field distribution is very important for optimizing the transducer efficiency of EMAT. Figure 3. EMAT components: (a) Spiral coil, (b) Cylindrical magnet (12.7 mm diameter and 28.5 mm height), (c) Schematic diagram of an EMAT probe demonstrates the spiral coil and cylindrical magnet with a diameter of 12.7 mm and height of 28.5 mm, used in this study.

Table 1. Material properties

Material	Elastic Modulus (GPa)	Poisson's Ratio	Density (kg/m3)	Thickness (mm) Stainless Steel - 316LASTM
	200	0.25	8000	3.048

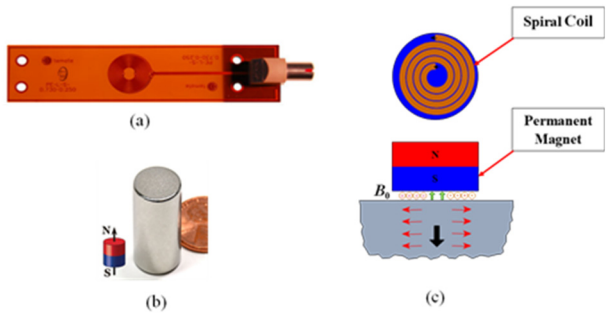

Figure 3. EMAT components: (a) Spiral coil, (b) Cylindrical magnet (12.7 mm diameter and 28.5 mm height), (c) Schematic diagram of an EMAT probe [4]

To excite the wave using the spiral coil, the dispersion curvature is used to find the excitation frequency. For a specific spiral coil, an approximate relationship between the optimal wavelength generated by the spiral coil and the spacing of the coil is given by:

$$\boldsymbol{\lambda} = OD - ID \qquad (1)$$

Where OD is the outer diameter, and ID represents the inner diameter of the coil. For the coil used in this study, the corresponding value for each is 12.7 mm and 0 mm, respectively. Typically, the matching condition should be satisfied between the wavelength of the Lamb wave mode and the coil's configuration for the design of a spiral coil in EMAT. The phase velocity and group velocity dispersion curves for lamb waves of a 3.048 mm thick stainless steel are shown in Figure 4. Dispersion curves for lamb wave modes of 3.048-mm stainless steel plate, (a) Phase velocity (b) Group velocity. When an EMAT is used to generate Lamb waves, the activated modes are selected based on the combination of the transducer's periodicity and the excitation frequency sent to the transducers. According to the fundamental relation, $\boldsymbol{\lambda} = c/f$, the wavelength or period generated by the spiral coil is related to the frequency and phase velocity. The sloped line in Figure 4. Dispersion curves for lamb wave modes of 3.048-mm stainless steel plate, (a) Phase velocity (b) Group velocity, represent the activation line at 12.7 mm wavelength and the

intersection of the line with the dispersion curves indicates preferential excitation points. There are several ways to select exciting modes for Lamb wave testing. In general, it is preferable to use only fundamental modes (*A*0 and *S*0). The simplest way is to limit the frequency below the cut-off frequencies of higher modes (i.e., excitation frequency between 1 kHz and ~600 kHz). As can be observed from the dispersion curvatures, A0 mode for this spiral coil is highly dispersive. As a result, S0 was selected for our inspection. The red spot in Figure 6 schematically indicates the activation zone when a tone-burst excitation having a ~401 kHz frequency is applied to the transducer. The group velocity of S0 for this frequency is 4924 m/s.

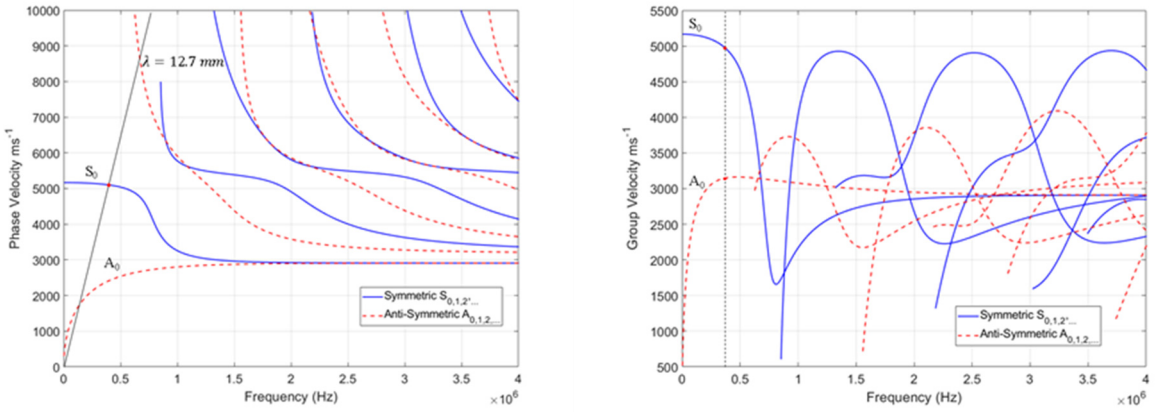

Figure 4. Dispersion curves for lamb wave modes of 3.048-mm stainless steel plate, (a) Phase velocity (b) Group velocity

On the gripper design side, a key question that arises is whether the coils should be conformed on the curved surface or not. In the following part, experiments were carried out to answer this question.

To integrate the robotic gripper and EMATs, the first step is to evaluate the tube curvature effect on the prop- erties of the generated Lamb waves. The curvature in test samples can substantially change the physical properties of the guided waves. In a circular sample, the curvature is defined to be the reciprocal of the radius as follows:

$$\kappa = \frac{1}{r} \tag{2}$$

Where $\boldsymbol{\kappa}$ is the curvature, and *r* is the radius of the sample. Preliminary tests were undertaken to describe the effect of curvature on Lamb wave excitation. To assess the impact of curvature on Lamb waves, tubes with different diameters (73.025 mm, 88.9 mm, and 114.3 mm) and a plate that represents an infinite diameter are considered (see Figure 5). All samples are 316 stainless steel with the same thickness (3.048 mm) to make sure that the measurement error is minimized.

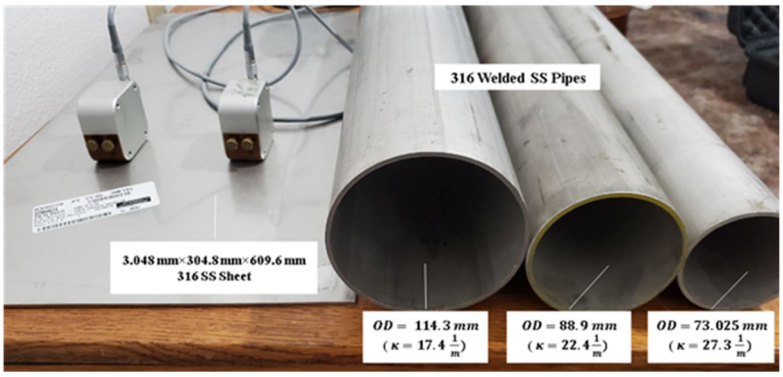

Figure 5. Hollow cylinders (pipes) and the plate used in this study

A PowerBox H data acquisition system was used to generate and receive Lamb waves using the designed EMAT. For all the following measurements, the EMAT is driven by a five-cycle tone burst with a center frequency of 401 kHz. The waves were excited using the computed burst frequency with the RX gain of 60 dB. Note that there is also a matching requirement for the receiver to the input preamplifier. According to the burst frequency, a bandpass filtering with the cut-off frequency of 325kHz to 475 kHz has been applied. In the discussion that follows, more details are provided.

Curvature effect on Lamb waves excitation using EMATs

There are two potential configurations for integrating the EMATs into the fingers of the LTI robot. In the first configuration, the coils should be conformed to the surface of the tube. This configuration requires a more sophisticated design for embedding the coils in the pads. In the second configuration, the coils can be placed on the flat surface of the fingers and it does not require embedding the coils into the pads. To investigate the effect of tube curvature on the Lamb wave propagation, the samples in Figure 5 were used with the two different configurations. Firstly, the coils were fully attached to the magnets. In this case, the coils are not conformed to the surface (i.e., there is no full contact between the coil and the curved surface). This case is named non-conformed throughout the text. In contrast, the second condition is the one that the coil is in full contact with the surface (named the conformed case). The schematic view of what is explained is shown in an arbitrary cross-section of the pipe in Figure 6(a).

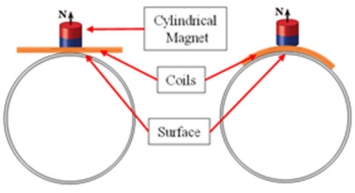

(a)

(b)

Figure 6. (a) Schematic view of coil configuration in EMATs testing: (i) non-conformed case (ii) conformed case, (b) Lamb wave excitation in pipes with spiral coils and cylindrical magnet (conformed configuration).

According to the ultimate gripper design, it is of interest to use similar coils and magnets (especially in terms of geometry and dimension). Therefore, the test was performed using a cylindrical magnet and the same coil (See Figure 3). As it is shown in Figure 6(b), the tests have been performed with the pitch-catch configuration (separate but identical transmitter and receiver) to mimic the communication between the eight EMATs used by the LTI robot. In these tests, no additional normal force is applied to the coils, and the magnets are just in full contact with the surface to avoid lift-off between EMAT transducer and substrate.

Figure 7 shows the received signals using a cylindrical magnet in non-conformed and conformed configurations. The signals are taken when the pair of EMATs is located 127 mm away from each other. In all cases, the arrival time of the selected Lamb mode can be identified using the group velocity determined from the dispersion curves. For example, the plate signal (Figure 7(a)) can confidently be identified as the *S*0 Lamb wave mode due to its correct arrival time at 52 μs. This figure also reveals that non-conformed coil results in slightly higher amplitudes compared to conformed configuration in all pipe samples. Figure 8(a) compares the two configuration responses with respect to the curvature of each tested pipe. On average, the amplitude of the received signal decreases by 8.6% when the coils are conformed to the surface. As a result, it seems that the conformed configuration does not improve the signal amplitude under the same circumstances. In the next part, this result has been considered in the gripper design for the LTI robot.

The time-trace in Figure 7 also reveals that the waves have different propagation velocities in each specimen. The group velocity of each case could be determined using the arrival time of the received signal from the generated wave pulse, (i.e., the time of arrival). Figure 8(b) shows the effects of curvature on the wave propagation velocity. As can be seen from this figure, the group velocities for the conformed and non-conformed configurations are almost consistent, which

means the coil conformation does not affect the wave velocity. However, the geometry of the samples can immensely change the group velocity. As shown in Figure 8(b), there is an inverse relationship between the curvature and the group velocity in specimens. Based on these tests and the complicated design requirement to embed and conform the coil of EMAT to the surface of tube in the LTI robot, the second configuration was selected to not conform the coils to the surface of tubes to be inspected.

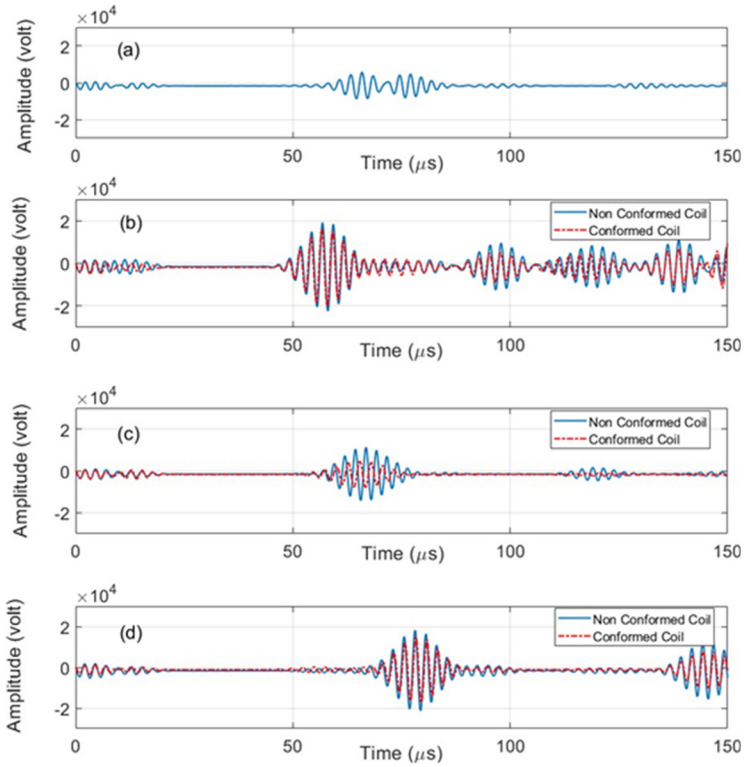

Figure 7. Lamb wave signals with spiral coil in non-conformed and conformed configurations: (a) plate (b) OD=73.025 mm, (c) OD=88.9 mm, (d) OD=114.3 mm

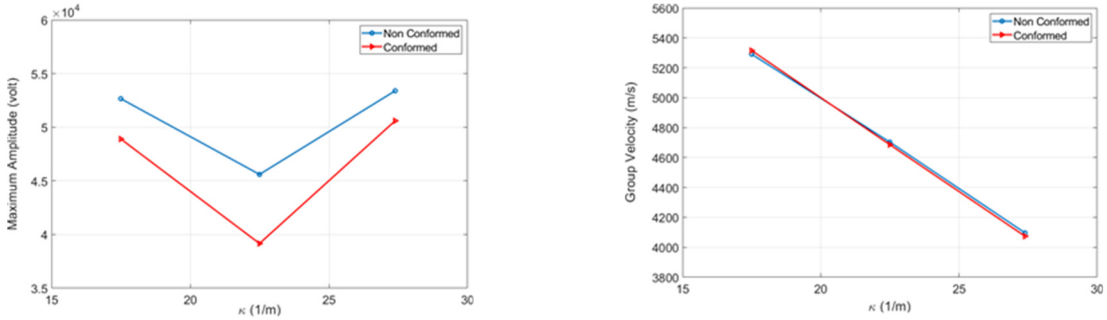

Figure 8. Effect of curvature on the wave propagation in materials with different diameters in relation with: (a) signal amplitude (b) group velocity

The sensing process has been accomplished using Lamb waves. To this aim, the *S*0 mode is applied to evaluate the performance of the gripper equipped with EMATs. Some preliminary data

were conducted to investigate the curvature effect on the properties of the Lamb waves. The obtained results reveal that the conforming of the coils necessarily does not increase the signal amplitude. Subsequently, the proposed gripper in non-conformed configuration was applied to perform an inspection over the pipes with different curvatures. Moreover, the received time-domain waveform generated by EMAT indicates the group velocities for the conformed and non-conformed configurations are almost consistent, while the curvature and the corresponding group velocity in the test samples are inversely proportional in both configurations. According to the inspection results, directly transmitted and received signals are successfully acquired in the time domain. Moreover, it is shown, as the diameter of the sample increases, the amplitude of the signal increases under the same circumstances. Finally, it is verified that the robotic ultrasonic system integrated with EMAT, can successfully generate Lamb waves with acceptable SNR levels for inspection of tubular components.

1.1.1. Dry coupling

The second option for exciting Lamb waves is to design Dry-couplant transducers. Initially, an experimental setup shown in Figure 9 was used at ASU to evaluate the effect of friction on Lamb wave excitation.

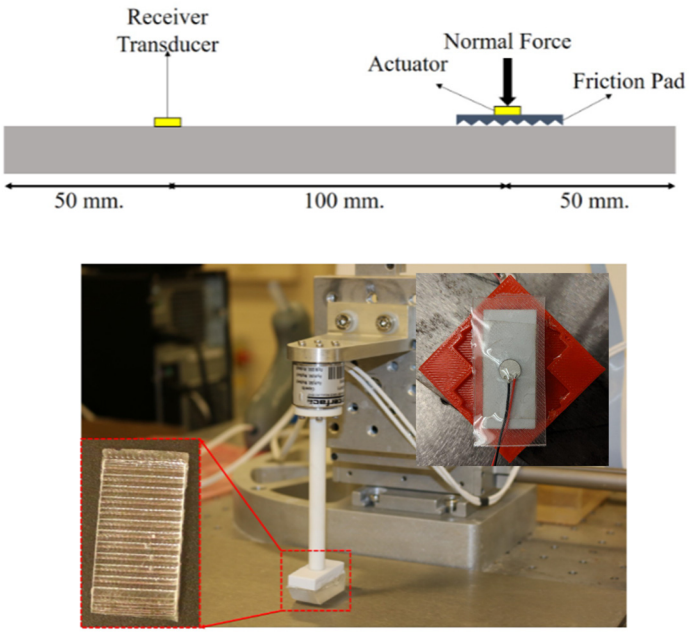

Figure 9. Experimental setup at ASU to evaluate effect of friction on Lamb wave excitation [10]**.**

The test perfumed in at ASU, revealed the potential friction-based excitation of Lamb wave using no couplant. A small compression system was fabricated at NMSU (see Figure 10) to test Lamb wave excitation capability using dry couplant.

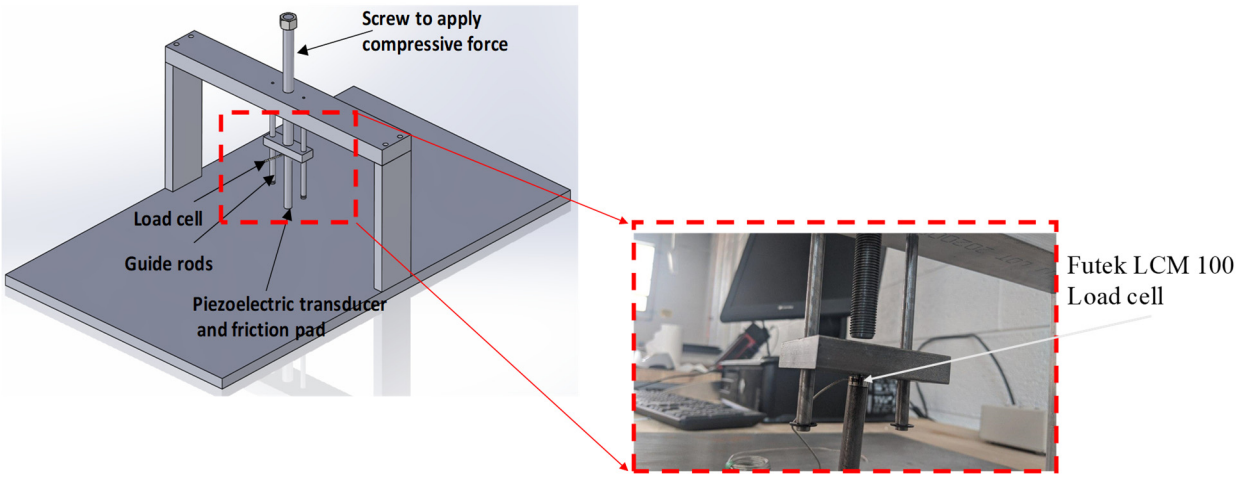

Figure 10. Compressive test setup

Since ultrasonic Lamb waves can transfer energy over a long distance, they have turned into a practical option for the integrity assessment of plate-like structures. Ultrasonic Lamb waves excited using the dry couplant (friction-based Lamb waves) have two fundamental characteristics. They are nonlinear and have dispersive characteristics. These two characteristics make the interpretation of received ultrasound waves a difficult task.

The multimode characteristic of Lamb waves hinders with an accurate selection of modes for different applications like corrosion or crack detection. Hence, decomposing multimode Lamb waves is important for better decision-making regarding structural integrity.

In this context, researchers rely on methods based on frequency domain analysis to decompose the multimode region of received Lamb waves. However, methods based on frequency domain analysis are heavily integrated with linearization since they are linear functions. As a result, the nonlinear information of received ultrasonic waves would be lost when methods based on frequency domain are applied. Also, methods based on frequency domain analysis fail to capture mode transitions since they are faint. Hence, to avoid mentioned shortcomings, in this project the phase-space domain analysis method is used. In this context, recurrence plot analysis is applied to detect the arrival time of different modes in received ultrasonic Lamb waves. Also, applying a recurrence plot would allow to extract the exact time of mode transitions.

Dispersion curves for a steel plate with a thickness of 4.8 mm are shown in Figure 11. According to this figure, at an excitation frequency of 800 kHz, 4 modes, S_0, A_0, S_1, and A_1, can exist.

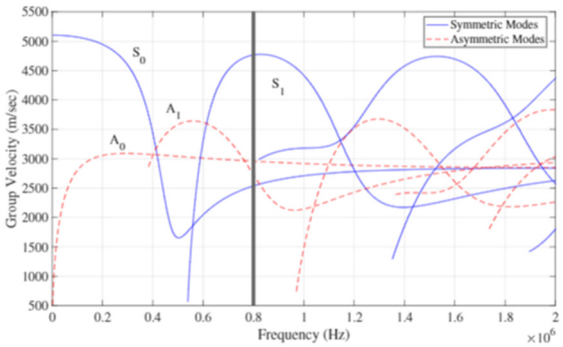

Figure 11. Normalized dispersion curves for steel plate with 4.8 mm thickness

Based on the group velocity of the four modes and distance between the transducers which is 10“, the arrival times of S_0, A_0, S_1, and A_1 modes are 39.41, 33.81, 20.98, and 36.67 µs, respectively. Figure 12 displays the recorded ultrasonic Lamb wave signal in the time domain and Figure 13 represents the frequency domain response (wavelet analysis). The inability of the time domain and the frequency domain in separating different lamb wave modes is clear from Figure 12 and 13. It is not possible to identify different modes and their transition using the time and frequency domain.

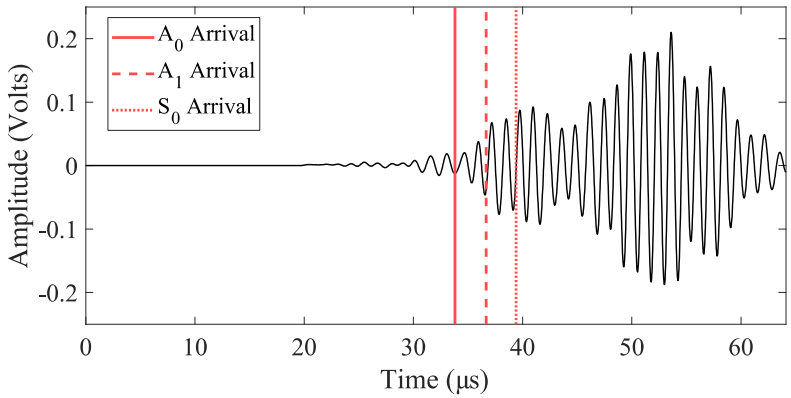

Figure 12. Received ultrasonic Lamb wave signal

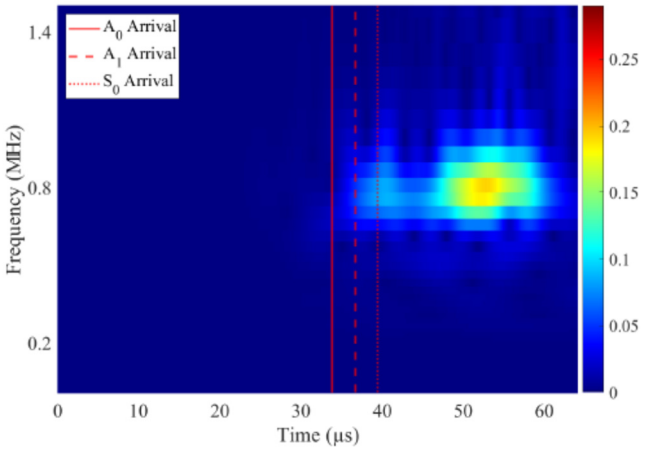

Figure 13. Frequency domain (wavelet) response of received signal

On the other hand, according to recurrence plots shown in Figure 14, the arrival times of different modes without relying on the frequency domain response or dispersion curves are clearly detectable. This is important since the recurrence plot is providing a magnifying window that makes mode detection a much simpler task. Also, the transition of different modes could be detected using a recurrence plot. This is important since leveraging recurrence plots would help with accurate mode decomposition which is not possible using methods based on frequency domain analysis.

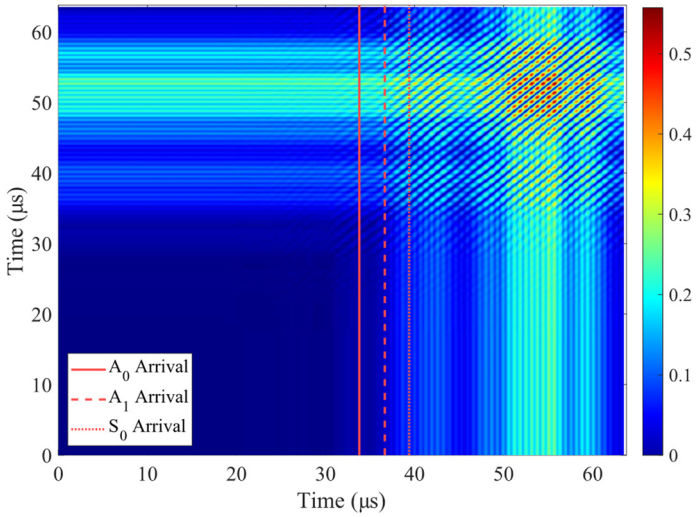

Figure 14. Recurrence plot of received signal

In another experiment, Ultrasonic Lamb waves with a center frequency of 0.4 MHz are excited while different normal forces are applied to actuator transducer. Since by increasing the normal force on the transducer, the friction between the transducer and steel plate increases, investigating this effect on the generation and propagation of ultrasonic Lamb waves is important. As displayed in Figure 15, the correlation between normal force and frequency can be seen. By increasing normal force, the frequency of received ultrasonic waves is decreasing significantly. It means that friction plays an important role in dissipating energy as well as in the generation of ultrasound Lamb waves.

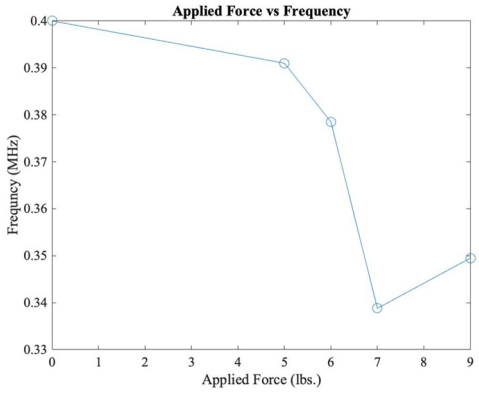

Figure 15. Correlation between the applied force on transducer and frequency of received ultrasonic Lamb waves

So far, the initial test perfumed at ASU, revealed the potential friction-based excitation of Lamb wave using no couplant. Since the dry-coupled medium that was used in this research has a wide range of friction coefficients with respect to its orientation and the applied normal load, the effect of friction on the transmission of Lamb waves was investigated. Large SNR is crucial when using Lamb waves in different applications such as defect detection and evaluation. Thus, investigating the effect of friction on the amplitude of generated Lamb waves is important when dry-couplant is used. Figure 16 and 17 display the correlation of friction force and friction coefficient with the maximum amplitude values, respectively. The results shown in Figure 16 and 17 verify that a larger friction coefficient and friction force are crucial for the generation and propagation of strong Lamb waves supporting the fact that the main mechanism to transfer mechanical energy using dry-couplant is friction. Interestingly, a linear behavior is observed between the transmitted ultrasound energy and the friction coefficient. The linear regression can be utilized as a tool to estimate the maximum expected amplitude of Lamb waves for certain normal loads for the designed PDMS pads used in LTI fingers. The sensitivity of Lamb waves to the friction coefficient highlights the importance of designing specific pads for varying surface conditions. It is concluded in this quarter that to achieve a high signal-to-noise-ratio when using dry-couplant, it is important to increase the friction coefficient by designing specific pads based on surface conditions.

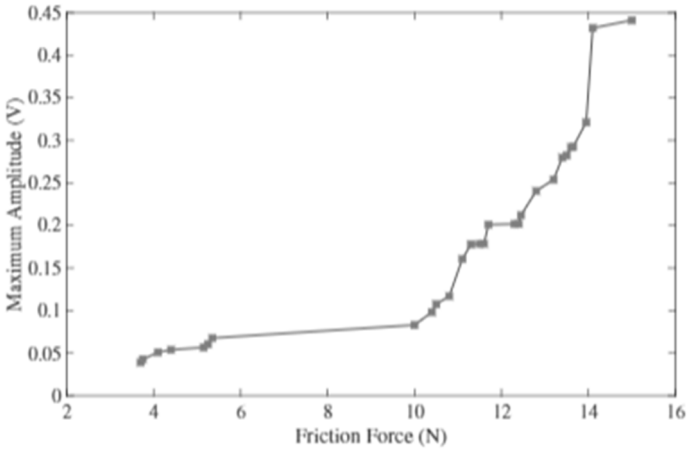

Figure 16. Correlation between friction force and maximum amplitude.

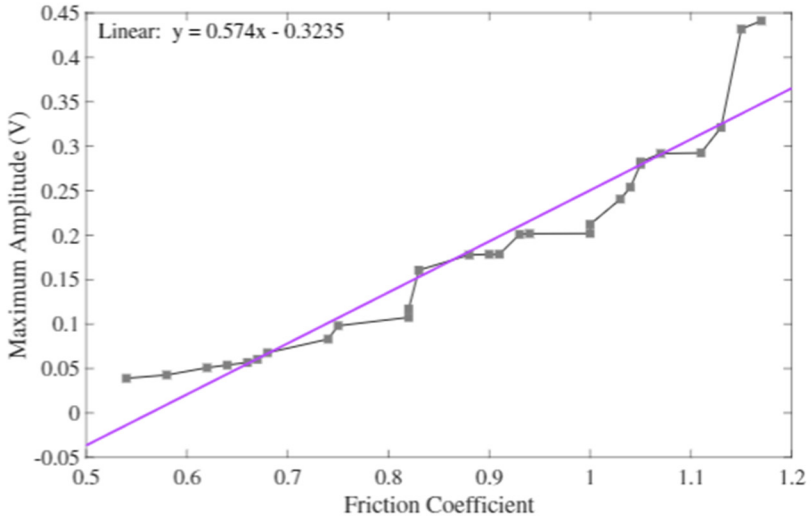

Figure 17. Correlation between friction coefficient and maximum amplitude [10]**.**

While the friction-based ultrasound excitation for dry couplant showed promising results [10], the research team decided to focus on EMAT. The friction-based ultrasound excitation needs further investigation to become practical.

1.2. Integration of the couplant-free ultrasound transducers into the robotic gripper

The LTI robot can travel along the boiler tubes without having to shut down the plant. The first version of the LTI robot (refer to robotic section in this report) comprises two grippers for grasping onto the tube and linear actuators, which connect the grippers and act as the spine of the robot allowing linear motion. The joints and actuators allow four degrees of freedom in each half of the robot including three rotational joints and one prismatic joint. There is another rotational joint connecting the two halves taking the total degrees of freedom to nine for the entire robot. These joints and actuators allow the robot to maneuver through any bends and turns that the boiler tubes might offer. In the first step, the modular design of the gripper which is used for testing would be discussed.

External grasping of a tube can be achieved through various robotic mechanisms like wheels, clamps, fingers, or limbs[1]. The biggest issue that most robotic grippers face is the modularity when it comes to grasping onto varying sizes of tube diameters. Another factor to consider is the placement of the EMAT sensors on the gripper for NDT. The addition of EMAT sensors means that wheeled grippers are not suitable for this application. That is why the idea of clamps and finger utilization is considered.

Gripper Design

The design of the robot gripper includes four fingers equipped with friction pads made out of poly-dimethylsiloxane (PDMS) for locomoting on the tubes. The detailed design of the gripper is

given in the following sections. Furthermore, EMAT sensors for inspecting internal defects in tubes are embedded in the extrusion embedded into the fingers. The difference between our gripper design and some of the novel grippers discussed earlier is that the curvature required to grasp onto the tube comes from the friction pads rather than the fingers or clamps. This gives the proposed gripper a sense of modularity when it comes to adjusting to different sizes of tubes. The curved surface of the friction pad allows it to maximize the contact surface between itself and the tube. Changing the gripper fingers each time for a new size of the tube is a cumbersome process. On the other hand, it is much simpler and more efficient to replace friction pads when they tend to wear off. The thickness of the friction pad between the tube contact surface and the EMAT sensor has been kept minimal (less than 1 mm) for the best results during NDT.

The gripper consists of 3 major components (see Figure 18):

1. Base plate: The base plate is a circular disc-shaped component, which is designed to accommodate the arch and the motors. It also acts as a connecting point for the gripper to the rest of the body of the LTI robot or the UR5 end-effector through the UR5 mount. The base plate consists of mounting provisions for 2 Dynamixel MX 106T motors and the arch. However, only one motor is required for the gripper finger actuation while the other provision is for the working of the LTI robot.
2. Arch: The Arch is split into two halves. The bottom half is connected to the base plate through six 8-32 size flat head screws. The bottom half and base plate combination act as the sturdy base for the gripper construction. The top and bottom halves of the arch are connected by six M6 bolts and nuts. These are designed to hold minor components such as bearings, shafts for finger actuation, and worm wheels.
3. Fingers: The fingers are the primary contact points for sensing. The gripper consists of 2 pairs of fingers, each pair connected to two separate shafts actuated by the same motor. Each finger consists of the EMAT sensor, friction pads, and other sensor provisions. The contact surface of the finger is designed to be flat, as the curvature required for the gripping is designed onto the friction pads.

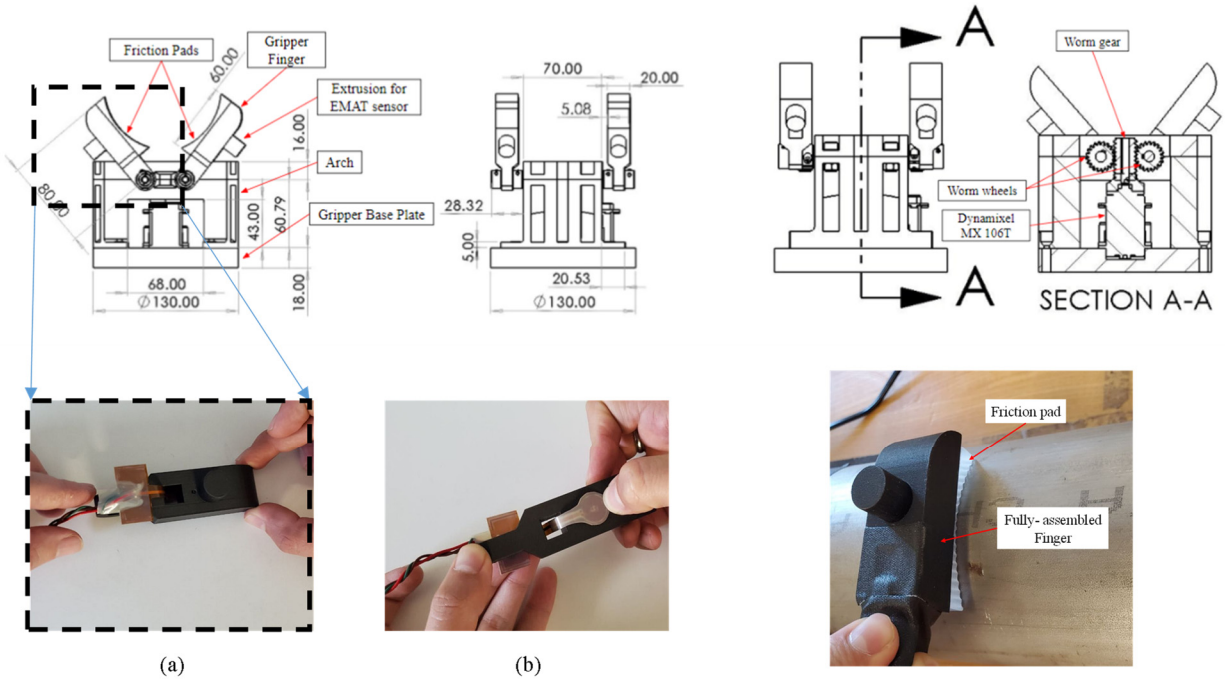

Figure 18. 2D view of the Gripper Design, (a) Front and Side view of the gripper (b) Cross-sectional view of the gripper [4]

These parts have been fabricated at NMSU through 3D printing using the Onyx material reinforced with fiberglass. While the initial intention to design this gripper was to be used in the LTI robot, the gripper is modular and can be used with different robotic platforms such as UR5 robotic arms. Figure 18 shows the first method for integrating the EMATs into the LTI fingers.

The mount for the gripper is a modular part. It can be detached from the gripper easily, and its design can be changed depending on the robotic arm. A UR5 manipulator was used for evaluating the performance of the gripper for inspecting tubular components using EMATs. The gripper is attached to the mount using six 8-32 size flat head screws. An illustration of the mount is shown in Figure 19. The mount is screwed onto the end-effector of the UR5 with the help of four M6 screws. This allows designers to position the gripper onto any part of the tube. A representation of the gripper operation along with the UR5 robotic arm is shown in Figure 19.

Figure 19. UR5 mount for the Robotic Gripper

The second version of the finger

From our previous observations, it has been found that reducing the distance between EMAT sensor and the testing pipe has produced better sensing results. Also, removing the friction pad between the sensor and the pipe can reduce noise as well. Hence, we have designed a new EMAT sensor holder (see Figure 20), which provides direct contact between the sensor and the pipe.

Figure 20 shows the testing procedure of the new holder. This test was done manually to provide insight into the gripper performance in terms of SNR before it is integrated into the LTI griper.

Figure 20. Testing the new gripper.

Figure 21 compares the received signal of the new and old sensor holders. The SNR increased by roughly 60%. This increase in the SNR can significantly improve the reliability and repeatability of inspection using LTI robot. The curved component in the new holder allows the sensor to stay steady in a fixed position and avoid coherent noise. The research team believes that this improvement can increase the sensitivity of the inspection to smaller flaws. In addition to the

improvement of the inspection capability of the LTI robot, this new design will allow the finger to have a larger contact area that can result in increased friction and as a result improved mobility.

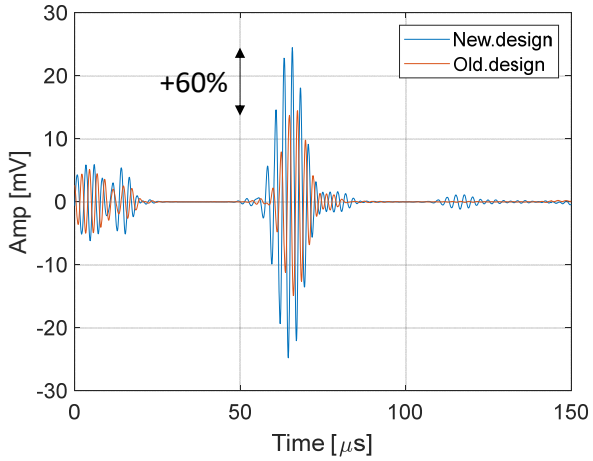

Figure 21. Compression of the received signal using the new and old holder design.

In-motion pipe inspection by gripper with EMATs

The dynamic movement of the gripper and its electrical components may affect the performance of the EMATs. To evaluate the performance of the gripper, in this part, the modular gripper that is integrated with EMATs is used for testing the pipes. The tests were undertaken in a semi-automatic way. As discussed, the designed gripper is attached to the UR5. This collaborative robot can be programmed to move a tool and communicate with other machines. A full laboratory setup for the pitch-catch experiments using the UR5 robot is shown in Figure 22. The movements of the gripper are controlled by the UR5 touchscreen control panel.

Once the initial tests of the UR5 were done and after DAQ system preparation, a code was created to have the robot move in a more autonomous way between two points to better mimic the movements of the LTI robot in action. This was done by using the pick and place option that is available with the UR5 software. Being allowed to use this form of coding simplified the process since all that needed to be done was manually move the robot to the desired place using the UR5 touch screen and lock the place. Therefore, the first position was above the pipe for clearance of the griper; then the UR5 would move down, allowing for the gripper to close and wait for a desired amount of time to permit for the tests to be done before it moved to a second location. Figure 22 shows the gripper grabbing the pipe surface while the EMATs on adjacent fingers are communicating. The robot system moves in a longitudinal direction. At the same time, EMATs perform the pipe inspection by transmitting and receiving Lamb waves.

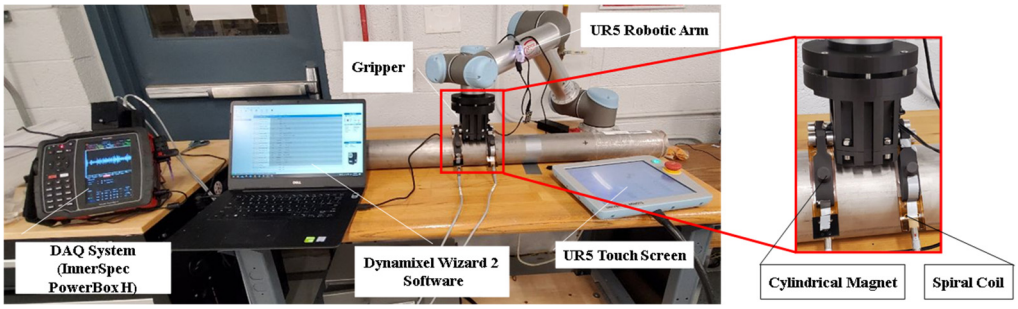

Figure 22. Experimental Setup for EMAT testing of the gripper [4]**.**

The grabbing process was prepared by using an open-loop feedback control where the gripper motors were controlled by Dynamixel Wizard. An *instruction packet* that contains the operating speed required for closing the fingers was sent to the pipe. Based on the signal characteristics (shape and amplitude), the operator sends another *instruction packet* to stop the motor and ensure that the gripper has latched onto the pipe correctly. After recording and collecting the data from the EMATs, the operator sent an *instruction packet* that allows the gripper fingers to open up. It is worth mentioning that based on the results obtained from the previous part, the sensing scenario has been performed in a non-conformed configuration.

As shown in Figure 23, according to the inspection results with the gripper, directly transmitted signals and received signals were successfully acquired in the time domain. The figure demonstrates that as the diameter of the sample increases, the amplitude of the signal increases under the same circumstances. This increase was because: 1. the conforming of the coils has less effect on the generation of Lamb waves, and 2. the geometry of the gripper has better functionality for the current pads for pipes around 114 mm diameter. Another interpretation of this statement has been demonstrated in Figure 24 indicating that the maximum amplitude linearly decreases as the curvature of the test samples increases.

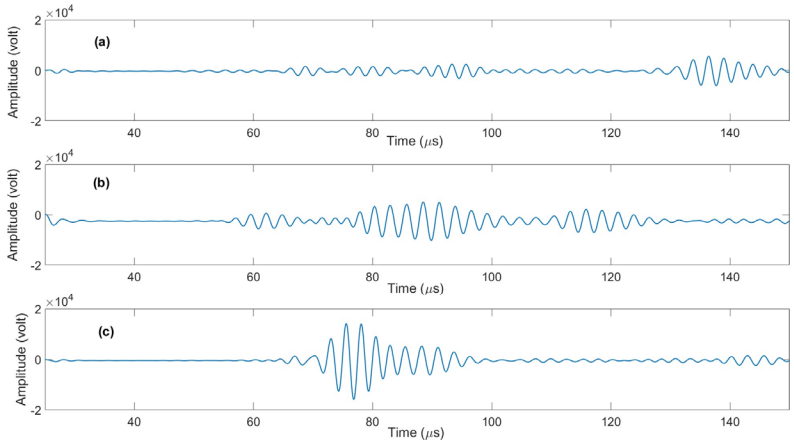

Figure 23. Lamb waves time histories in different pipes: (a) OD=73.025 mm, (b) OD=88.9 mm, (c) OD=114.3 mm [4]

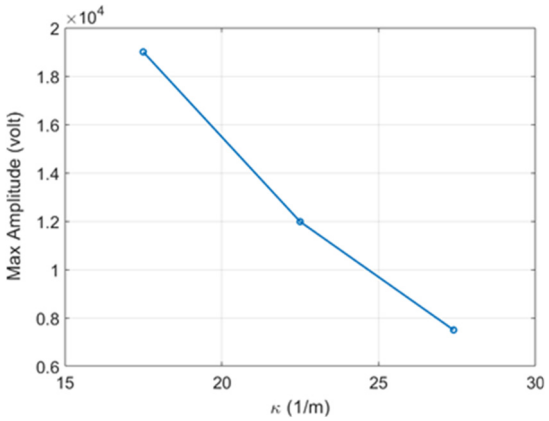

Figure 24. Relation between the signal amplitude and the samples curvature [4]

The design and integration of the EMATs were completed in this section. The next step is to use the collected data to detect and localize defects.

1.3. Data-Driven defect detection

To detect and localize defects such as corrosion and cracks, two approaches are considered in this research. Initially, a multi-helical imaging approach was proposed to detect defects between the grippers. The complexity of the EMATs-generated signals and the potential complex geometry of tubular components in power plants led us to use a more advanced data-driven approach based on deep learning. In the first step, the research team developed a method to estimate the coverage area of a network of sensors in plate-like structures (a pipe or tube can be considered as a wrapped plate). This will allow the LTI robot to estimate the coverage area between the grippers based on the combination and position of the eight EMAT sensors used by the LTI robot.

1.3.1. Lamb wave-based imaging and coverage area estimation

The proposed framework for sensor network coverage prediction proceeds in three primary steps: (1) numerical modeling, (2) back-scattered field estimation using nonlinear regression, and (3) coverage estimation using superposition. The first step numerically simulates cases of wave propagation and wave-crack interaction at different angles of incidence using FEM. One of the assumptions is that the geometry of the defect (e.g. critical defect) is known since the critical defect with acceptable dimensions is usually provided by material and design engineers. In this paper, the critical defect is assumed to be a partial crack with a 15 mm length and a depth that is one-third of the plate thickness. To estimate the back-scattered field of a wave from the crack with arbitrary angles of incidence, displacement field from a few FEM results are obtained. The second step fits a set of predicting functions to the displacement fields that were exported from the FEM models using nonlinear regression. In the third step, these functions are implemented to estimate the coverage area for any given combination of a transducer, receiver, and potential crack locations. By using superposition, coverage areas of different sensor pairs are fused

together to form the coverage area of a sensor network. A schematic view of the proposed framework is shown in Figure 25.

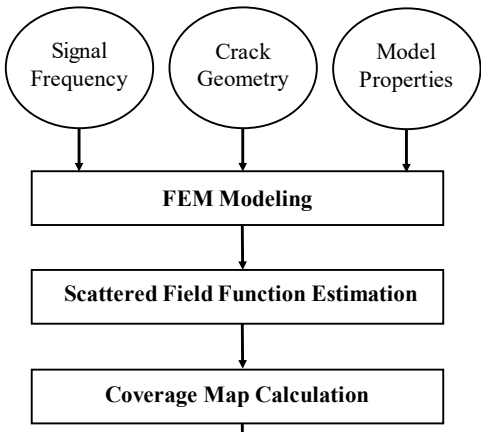

Figure 25. Summarized simplified framework for sensor network coverage prediction [11]**.**

FEM Simulation of the Back-Scattered Field

The proposed framework for coverage area estimation in this section is devised with the assumption that data from back-scattered reflections (i.e. reflections from a defect) will be used in the imaging method to visualize the defect location. Since the imaging procedure will be based on a reflected waveform, the back-scattered field of the critical defect is needed to be used in coverage area estimation. Researchers have proposed analytical solutions to determine interactions between certain types of cracks and Lamb wave modes to determine back-scattered fields [12][13]. When there is no analytical solution for a generic case, a numerical solution such as FEM is necessary. Three-dimensional FEM simulations in ABAQUS platform [14] were used in the past to generate back-scattered fields and the same approach is incorporated in this paper. One contribution of this paper is to find a simplified framework to estimate the back-scattered field of Lamb waves using results from only a limited number of FEM models in which the plate and the partial crack is simulated.

As previously mentioned, in this proposed framework the critical defect must be known. The critical defect is assumed to be a partial crack with a minimum length of 15 mm (or larger), a width of 1mm, and depth of 1mm. To simulate the propagation of the Lamb wave, a 6061-T6 aluminum plate with dimensions of $2000\ mm \times 2000\ mm \times 3\ mm$ was modeled with material properties as follows: elastic modulus $E = 69\ GPa$, density $\rho = 2700\ kg/m^3$, and Poisson's ratio $\nu = 0.3$[14]. For the FEM simulations and experimental setup to agree with each other, an operating frequency must be chosen to generate Lamb waves. The operating frequency was set to 400 kHz based on a tuning process that will be explained in section 5. To generate Lamb waves, a point-load source was defined at one node on the top surface of the plate. A tone burst with five cycles and a center frequency of $400\ kHz$, with a maximum amplitude of $1 \times 10^{-4}\ N$ normal to the plate surface was used as the excitation signal. The corresponding wavelength for A_0 and S_0 modes are 7.5 mm and 12.5 mm, respectively. The partial crack was introduced by removing corresponding mesh elements. The critical partial crack can have an arbitrary orientation; hence to model different angles of incidence, the wave source was moved to different locations on the

circumference of a circle having a radius of 400 mm, with the midpoint of the partial crack at its center. A schematic view of the FEM model is presented in Figure 26. Five models with different incident angles of $0, {}^{\pi}/_{12}, {}^{\pi}/_{6}, {}^{\pi}/_{4}$ and ${}^{\pi}/_{3}$ radians were generated.

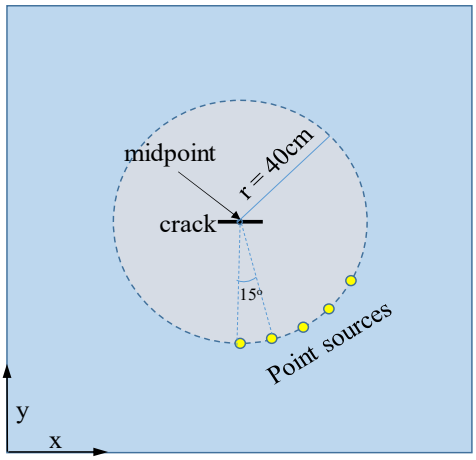

Figure 26. Schematic of FEM model.

Explicit time integration was used with linear brick elements of 1 mm to ensure the presence of at least eight elements per wave length [15]. Furthermore, with the 1 mm brick element, the requirement for a length-to-thickness ratio of less than 1.25 is met. The maximum time-step limit was selected as l/c, where l is the element length and c is the largest possible wave speed (e.g. $6420\ {}^{m}/_{s}$ for the bulk longitudinal wave speed), to ensure stability of the explicit integration scheme. Figure 27 shows two snapshots of the FEM simulation at different times for Lamb waves reflected from the partial crack. In Figure 27, the incident wave direction is perpendicular to the crack orientation. One can clearly observe both the back-scattered wave and forward-shadowing effects. The displacement field ($|d|$) presented is the resultant of three components of the displacement field in x, y, and z directions.

Back-scattered fields were obtained from FEM simulations based on a baseline subtraction scheme. For each incidence angle, two models were created. In the first, baseline data was obtained from the model without the crack; the simulation was repeated in the second model, which contained the partial crack. Propagation of reflected waveforms was obtained by subtracting intact plate model displacement fields from their defected counterparts at selected time steps. Lamb wave back-scattered fields were obtained by allocating the maximum displacement field among selected time steps to each node. In total, ten simulations with five different angles of incidence were performed to investigate the effects of the angle of incidence on the resulting back-scattered field. A simulated back-scattered field resulting from a crack with a zero-degree incidence angle is presented in Figure 28.

This figure illustrates the main reflection lobe as well as many side and edge reflection lobes.

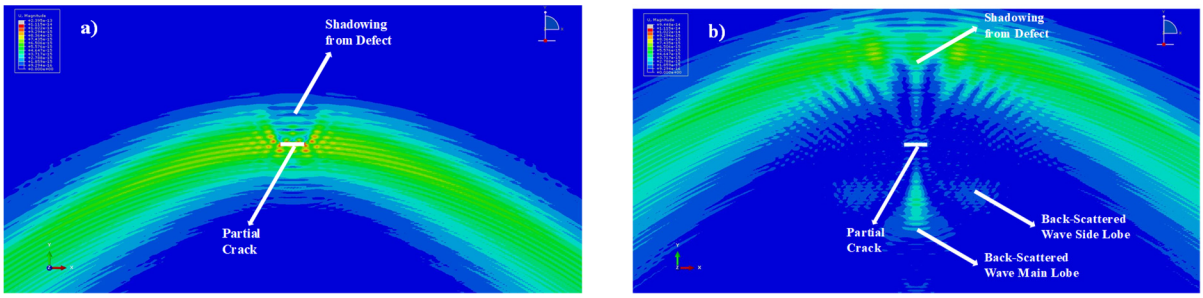

Figure 27. Finite element simulation results. a) Incidence of wave to a partial crack. b) Reflected wave propagation.

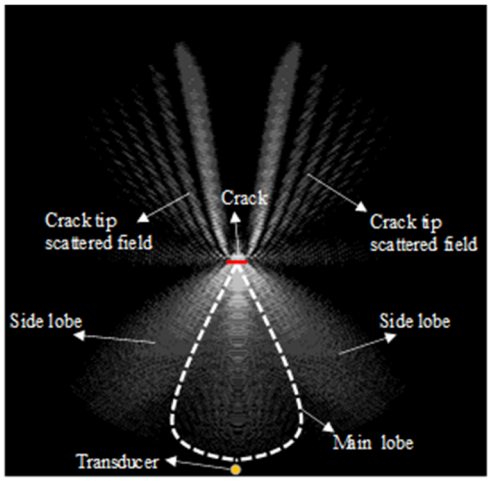

Figure 28. Back-scatter field for a crack with an angle of incidence equal to 0o.

To estimate a reflection back-scattered field function, needed for the next step of the analysis, only the main reflection lobe that carries most of the reflected energy is considered. It should be noted that the estimation of coverage is conservative since the function obtained represents a smaller field (main lobe only) and ignores tip reflections. Furthermore, since the imaging algorithm that was used to detect the crack is based on the reflection of Lamb waves, the reflection scatters field (back-scattered field) was considered while the forward sound field due to shadowing was neglected.

The same procedure was followed for all five incidence angle models to simulate the back-scattered fields. The resulting back-scattered fields are utilized to construct a two-dimensional function that represents the back-scattered field; the function can be used to compute the coverage area of varying sensor combinations.

Back-Scattered Field Estimation

It is impractical to numerically determine the back-scattered field of every possible scenario of crack location and transmitters. Hence, in this section, a function is proposed to estimate back-scattered fields based on the simulations performed. The back-scattered field of a wave changes in two directions (i.e. radial (r) and tangential (s) directions, as shown in Figure 29). The general form of the proposed back-scattered field function is presented in equation (3).

$$Z_\theta^l(r,s) = A(l,r,\theta) \times e^{-\left(\frac{s}{c(r)}\right)^2} \quad (3)$$

Where $A(l,r,\theta)$ is the displacement field in millimeters, r is the distance from the center of the crack in millimeters, l is the distance from the source to the crack in millimeters and θ is the angle between an incident line and a line perpendicular to the crack in radians (see Figure 29). In equation (3), the first term includes the directionality and attenuation of the incident wave based on beam-spreading effects, while the second term considers the attenuation of the Lamb wave reflection. It should be noted that this proposed function ignores the nearfield effects that can be seen in the FEM results, while giving an acceptable estimation of a back-scattered field in the far- field region (e.g. the far-field starts at a distance of approximately two wavelengths away from the sound source). In the radial direction (r) the amplitude of a reflected wave drops rapidly as the reflection wave front propagates away from the crack. Detailed discussion of the directionality effect of Lamb wave reflection from crack has been provided in the literature.

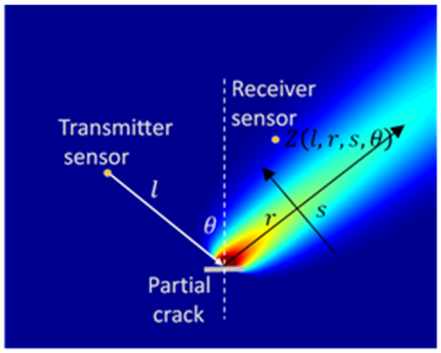

Figure 29. Parameters of the function used for back-scattered field estimation.

A reciprocal function is proposed in equation (4) to estimate the back-scattered field in the radial

$$A(l,r,\theta) = \frac{1}{l+1} a(\theta) r^{b(\theta)}, b(\theta) < 0 \quad (4)$$

direction (r direction shown in Figure 29.

Since maximum amplitudes for each coordinate at discrete time steps were used to build back-scattered field maps, a magnitude of Hilbert Transform of each slice of 2D data was used as input to maintain consistency in numerical results before a function could be fitted properly to the

numerical results of the FEM models. Nonlinear parameter estimation algorithms were used to estimate the parameters of the radial attenuation function. Figure 30 illustrates the results for an incidence angle of $\theta = {}^{\pi}/_{6}$ radians. shows results for different angles of incidence (θ).

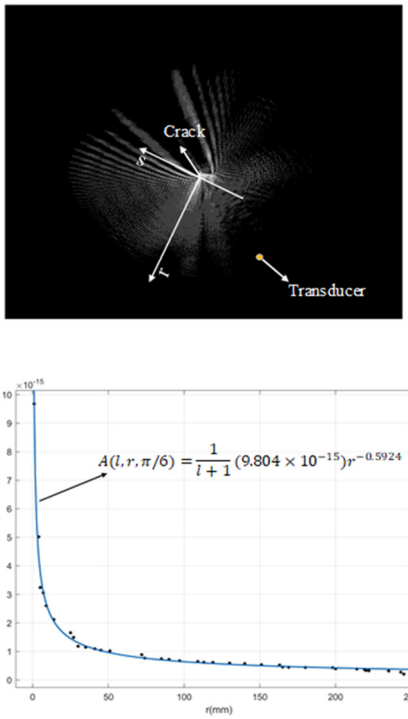

Figure 30. 30-Degree *A(.)* data

$$A(l,r,\theta) = \frac{1}{l+1}\alpha_1 e^{\alpha_2\theta} \times r^{(\beta_1\theta^2+\beta_2\theta+\beta_3)}, 0 \le \theta < \frac{\pi}{2}, r \ge 0 \quad (5)$$

$$c(r) = \gamma_1 r^{\gamma_2} \quad (6)$$

$$Z_{\theta}^{(l)}(r,s) = \frac{1}{l+1}\alpha_1 r^{(\beta_1\theta^2+\beta_2\theta+\beta_3)} e^{\left[\alpha_2\theta-\left(\frac{s}{\gamma_1 r^{\gamma_2}}\right)^2\right]}, \ 0 \le \theta < \frac{\pi}{2}, r \ge 0 \quad (7)$$

The two functions $a(\theta)$ and $b(\theta)$ in equation (4) were assumed to be the parametric functions

given in equation (5) and their parameters were estimated by regressing columns a and b against the first column of the same table. In equation (7), $A(l,r,\theta)$ is the displacement field in millimeters that is considered to be representative of the output signal.

Table 2 shows values for the parameters used to describe the $Z_{\theta}^{(l)}(r,s)$ function. It should be noted that these values are estimated for the specific models described in the previous section. For a different application, one can repeat the same procedures in this framework for modeling and parameter estimation.

Table 2. Parameters of back-scatter field function.

α_1	α_2	β_1	β_2	β_3	γ_1	γ_2
2.81×10^{-14}	-2.28	-0.33	0.78	-0.71	12.76	0.35

Table 3. Parameter estimation results for radial attenuation.

θ	a	b	SSE (Sum of Squared Errors)	R-square
0	2.892e-14	-0.7245	1.122e-29	0.9868
$\pi/12$	2.020e-14	-0.6490	1.692e-29	0.9190
$\pi/6$	9.804e-15	-0.5924	9.629e-31	0.9912
$\pi/4$	6.086e-15	-0.3739	4.443e-31	0.9883
$\pi/3$	5.125e-15	-0.3563	4.824e-31	0.9783

In the perpendicular direction (s) the back-scattered field spreads in an exponential manner [16]. Figure 31 (b) shows this behavior in 36 different sections alongside the radial direction. Again, a Hilbert Transform had to be used to extract the displacement amplitude at FEM discrete slices before the parameter estimation procedure could be performed. A power function was fitted to 36 estimated values for $c(r)$ in equation (3) in different sections to determine the unknown function $c(r)$ in equation (1). The parametric function $c(r)$ is presented in equation (6), in which r is the distance from the crack midpoint in the direction of reflection in millimeters.

The final 2D back-scattered field function is presented in equation (7) in which $Z_{\theta}^{(l)}(r,s)$ is displacement field at any given point of a plate domain.

For a crack with zero-degree orientation, Figure 31 (c) shows how well this function can estimate the back-scattered field obtained numerically (Figure 31 (a)). In the next step, this function will be used to estimate the back-scattered field for the critical defect at an arbitrary location with respect to a transmitting sensor.

Coverage Map

Figure 29 shows the schematic configuration of a combination of the transmitting sensor and crack inclination on a plate as well as the estimated back-scattered field of the propagating wave calculated based on $Z_{\theta}^{(l)}(r,s)$. For a fixed crack inclination, the 2D scattered field function can be

mapped to an ordinary Cartesian coordinate system and be rewritten as $Z_{\alpha}^{(t,c)}(x,y)$ in which the subscript α refers to the angle between the crack and a horizontal line, and superscripts t and c refer to transmitter and crack coordinates, respectively.
To construct a coverage map for a transmitter/receiver pair, the intensity of each pixel is simply

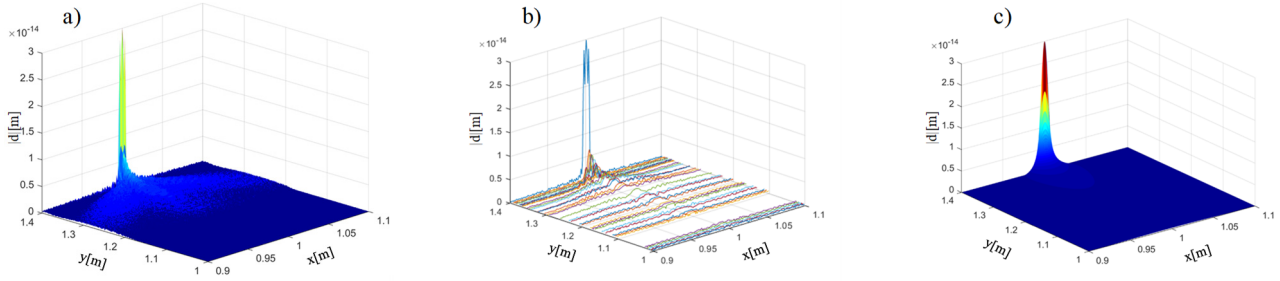

Figure 31. a) Result from FE model. b) Data nodes used for parameter estimation. c) Estimated function.

assigned by using equation (8) and calculating the value of the scatter field function at the receiver location, with the crack located at the coordinates of the desired pixel. In equation (8), subscripts t and r refer to the transmitter and the receiver, respectively and (x_r, y_r) is the coordinate of the receiver. As two examples, Figure 32 shows coverage maps for a transmitter/receiver pair for 0° and 45° cracks. The coverage map of a sensor network can be derived by superimposing coverage maps of every possible transmitter/receiver pair in the network. To take into account the pulse-echo mode, in addition to through-transmission mode, one can consider transmitter/receiver pairs at the same location. The entire procedure of coverage map estimation is summarized in Figure 33.

$$C_{\alpha}^{t,r}(x,y) = Z_{\alpha}^{t,c|_{x,y}}(x_r, y_r) \tag{8}$$

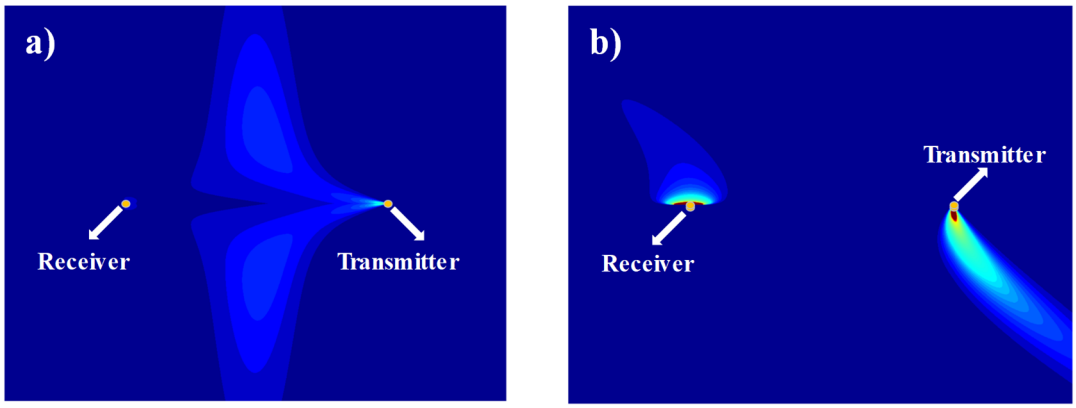

Figure 32. Coverage area of a transmitter/receiver pair for a) α=0o crack. b) α=45o crack.

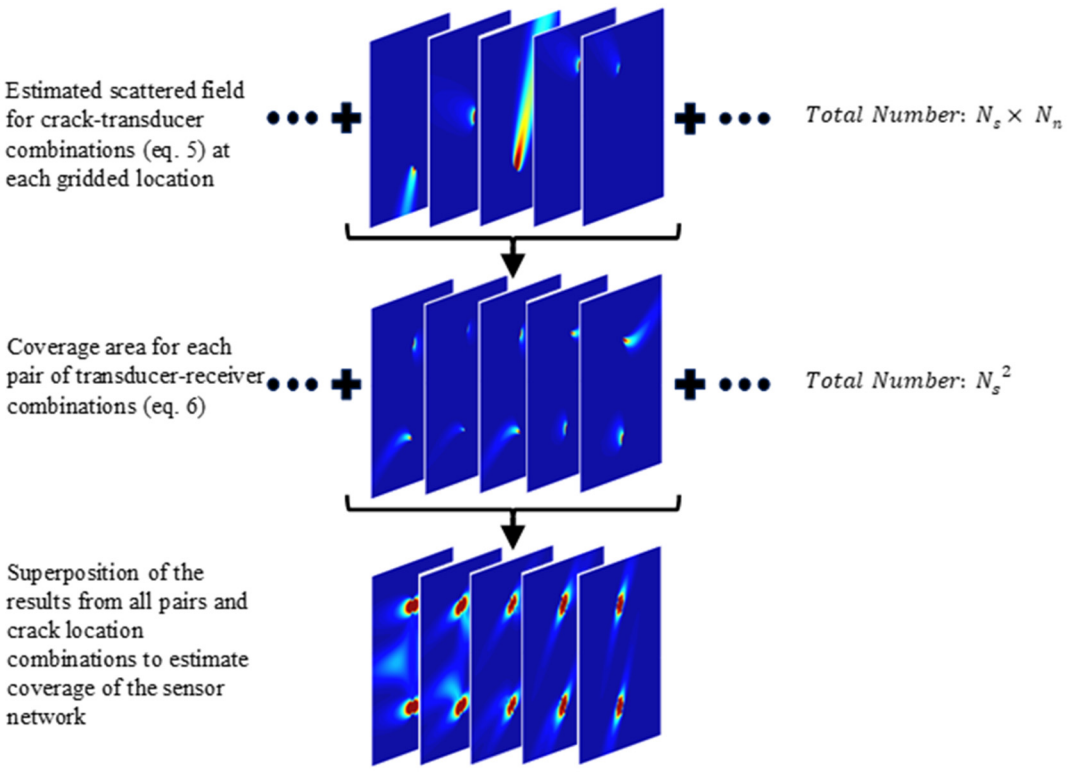

Figure 33. Summary of superposition step to estimate the coverage of sensor networks.

The coverage area is a function of the number of sensors and the geometrical arrangement of the sensor array. To provide insight into the estimated coverage maps of a few simple sensor arrangements, Figure 34 and 36 present examples of the coverage areas for sensor networks consisting of one to five transducers for cracks having four different inclinations. In these figures, the confined coverage area is defined by a -17dB intensity threshold, and the percentage is calculated as the ratio of the confined area to the area of a 3000×3000 mm plate (unwrapped pipe). As it is shown in Figure 34, in the case of a single-sensor arrangement, the shape of the coverage area is not affected by the inclination of the crack. By increasing the number of sensors to two, the coverage area is increased by five times when the crack inclination is α=0. In the case of inclinations α=π/6, α=π/4, and α=π/3, the increase in the coverage area is almost four times that of the case with a single transducer. This observation shows that the coverage area of a sensor network depends on both sensor network geometry and crack inclination, and it is not necessarily a linear function of the number of sensors. By increasing the number of sensors from two to three, there is a slight increase in the coverage area for the case of α=0. This increase in the coverage area, however, for crack inclinations of α=π/6, α=π/4, and α=π/3 is almost two times that of the dual-sensor arrangement. Again, it can be inferred that both sensor arrangement geometry and crack orientation affect the coverage area. The most efficient sensor arrangement among those presented in Figure 34 is a square-shaped quadrupole-sensor network. Because of the existence of straight and diagonal transmitter/receiver pairs, this arrangement works best for all crack orientations. In this case, the coverage area has an almost 60% increase compared to triple arrays of the transducers for all inclinations.

Figure 35 shows the quintuple arrangement of the sensors. In this case, the transducers are in four different compact arrays: linear, L-shaped, cross-shaped, and pentagon array. A similar procedure has been implemented to compute the coverage area of the plate. By comparing these cases, it is inferred that the linear arrangement of the transducer results in the greatest coverage area value. In this case, however, it is apparent that as the crack inclination increases, the coverage area decreases. Since the orientation of the crack in reality is unknown, a sensor arrangement that can provide a reliable coverage for all orientations is preferable.

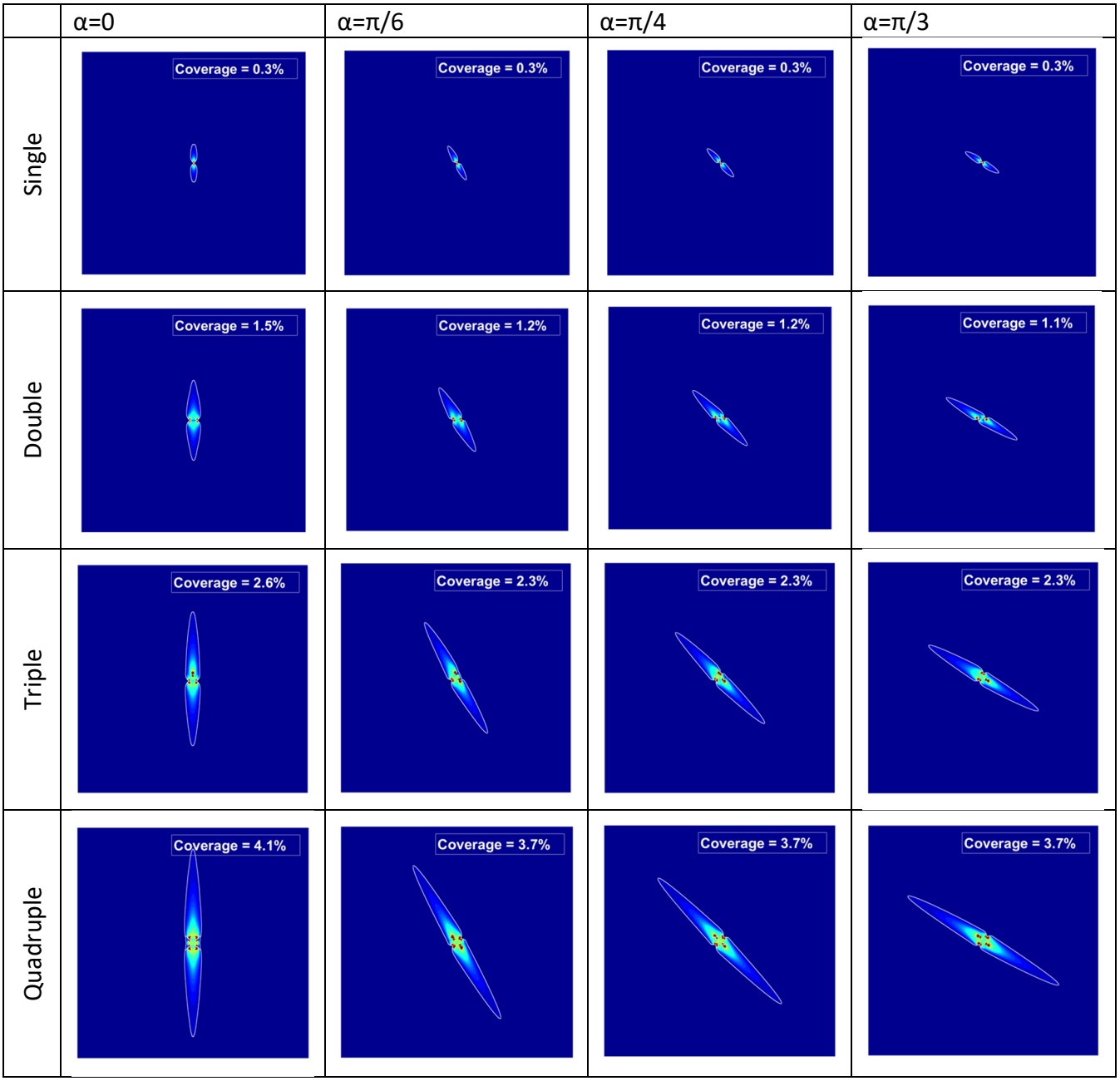

Figure 34. Coverage areas of different sensor arrangements for various crack inclinations.

Among these proposed quintuple arrangments, the pentagon array comes next in terms of the largest coverage area, but it is more reliable since it provides consistent coverage areas for all crack orientations. L-shaped and cross-shaped almost result in the same coverage area. In all of the last three arrays, a constant decline in the coverage area for the crack inclination of $\alpha=\pi/6$, $\alpha=\pi/4$, and $\alpha=\pi/3$ was observed. The LTI robot sensor configuration (Quadruple) is also robust in terms of coverage area.

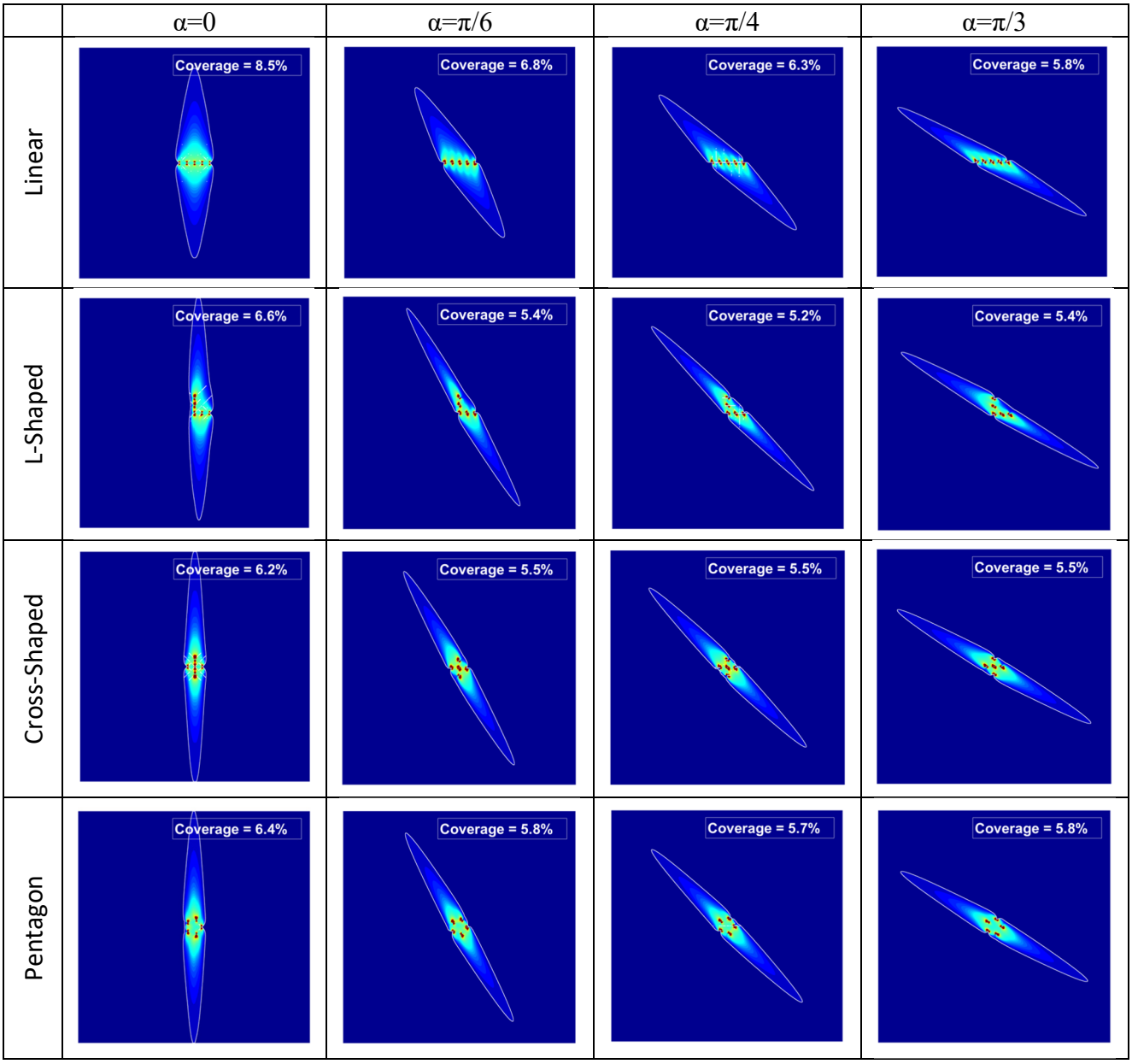

Figure 35. Coverage areas of different quintuple compact arrays for various crack inclination.

The previous discussion about Figure 34 and 36 did not consider the number of transducers. To take this important factor into account for the evaluation of the effects of the sensor arrays on coverage area, the coverage area percentage per transducer for different cases provided in this study, is presented in Figure 36. This figure shows a clear trend that indicates as the number of sensors increases from one to five, the coverage area per sensor increases. The results regarding the quintuple arrangement of the sensors appear to be disputable. Figure 36 pinpoints that the result of the linear arrays of the five transducers is superior to the others, especially in the case with zero-degree inclination. On the other hand, the pentagon compact array results in a broadly consistent, large coverage area for various crack inclinations. According to these results, the combination of the linear and pentagon arrays of the sensors was considered in the experimental study in the next step.

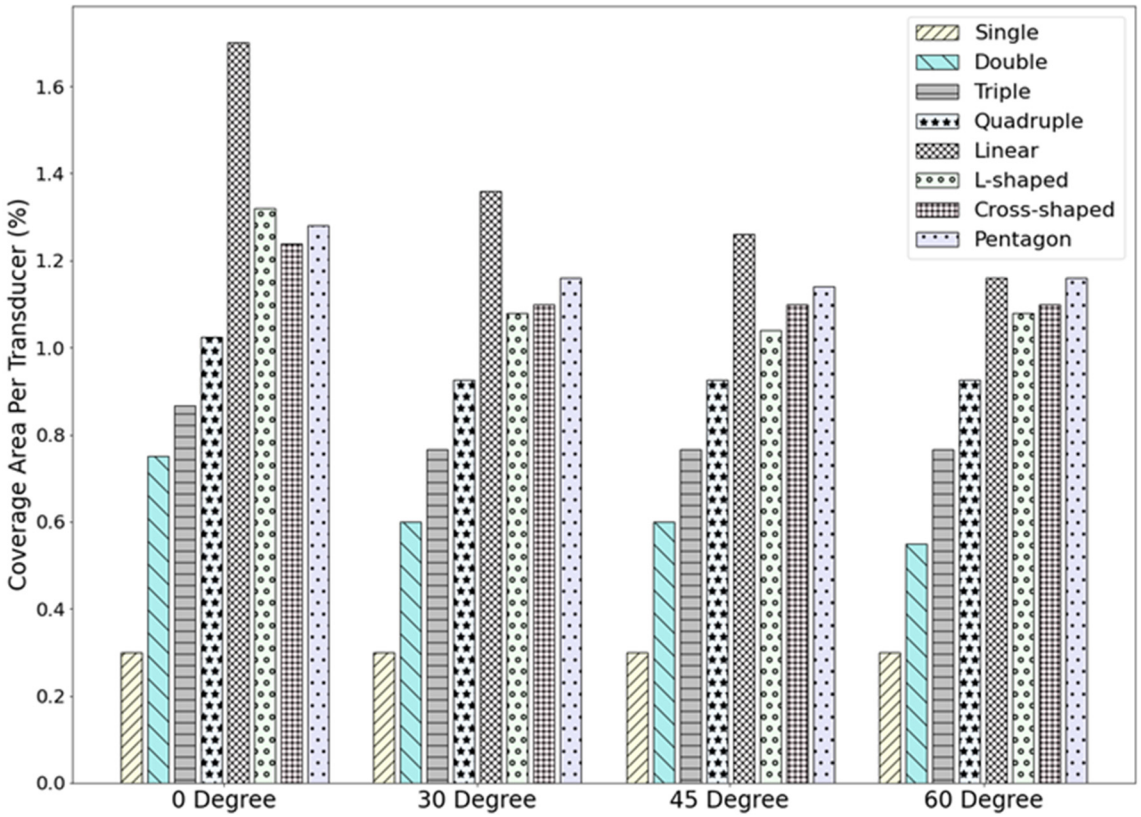

Figure 36. Coverage area per transducer for different sensor arrangements and various crack inclinations.

Experimental Validation

Numerical coverage area estimation based on the proposed framework was experimentally verified by using a network of permanently attached PZTs. To perform this experiment, a 6061 aluminum alloy plate with dimensions of 763 mm × 914 mm × 3 mm was chosen, which matches the plate used in FEM simulations, in terms of dimensions and mechanical properties. In this experiment, circular PZT sensors of 6mm diameter and 1mm thickness were used. Two clusters of PZT sensors, right and left, each consisting of seven sensors, were glued to the plate surface. The coordinates of the sensors are listed in

Table 5. Figure 37 shows the experimental setup. The crack was saw-cut with a controlled machining tool. The critical crack specifications are listed in
Table 4.

Table 4. Crack specifications.

Center Coordinates	Crack Length	Crack width	Crack Depth	Crack Angle
x_c=0mm, y_c=-242mm	15mm	2mm	1.5mm	0°

Table 5. Coordinates of PZTs on the plate.

Left Cluster			Right Cluster		
Mark	x(m)	y(m)	Mark	x(m)	y(m)
L_0	-0.203	0.000	R_0	0.203	0.000
L_1	-0.203	0.032	R_1	0.203	0.032
L_2	-0.176	0.016	R_2	0.176	0.016
L_3	-0.176	-0.016	R_3	0.176	-0.016
L_4	-0.203	-0.032	R_4	0.203	-0.032
L_5	-0.231	-0.016	R_5	0.231	-0.016
L_6	-0.231	0.016	R_6	0.231	0.016

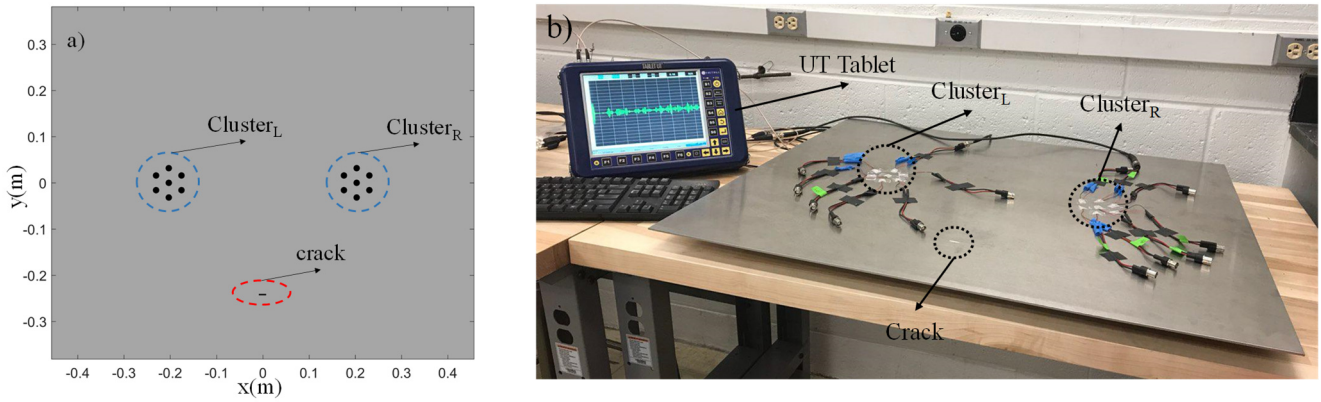

Figure 37. Experimental setup. (a) Schematic picture. (b) Specimen and UT tablet.

Coverage areas for three different sensor network arrangements interacting with a horizontal crack as the critical defect are estimated using the proposed framework. The three sensor networks (e.g. left cluster only, right cluster only, and combined left and right clusters) and their estimated coverage areas are illustrated in Figure 38. It is expected that the crack is only detectable when both clusters work together (Figure 38(c)). It is worthwhile to note that the network coverage area significantly increases if the two sensor clusters communicate with each other. To verify the accuracy of the estimated coverage area, the critical crack is positioned in the area between two clusters. The location of the crack in the experimental setup is intentionally

selected in an area where both single cluster arrangements are predicted by the proposed framework to be blind, but ensuring that the crack will be covered by the sensor network containing both clusters (Figure 38).

To select the operating frequency, two sets of curves, namely dispersion curves and tuning curves, should be investigated. Dispersion curves (Figure 39) illustrate the group velocities of different propagating wave modes as a function of frequency and plate thickness. These curves are used for mode selection by means of selecting excitation frequencies that are beyond the first cutting frequency to limit the excited modes to fundamental symmetric S_0 and antisymmetric A_0 Lamb wave modes. Tuning curves shown in Figure 40, on the other hand, provide the amplitude of different modes as a function of the excitation frequency. An appropriate frequency is one that achieves both a high signal-to-noise ratio and eliminates higher-order Lamb wave modes. Figure 40 shows the tuning curves for S_0 and A_0 Lamb wave modes. To draw tuning curves, signals at different frequencies, ranging from 50kHz to 600kHz, were transmitted in a pitch-catch mode. In a round-robin fashion, A "MISTRAS UT Tablet" was used for generating five-cycle tone burst signals, as well as receiving and storing them.

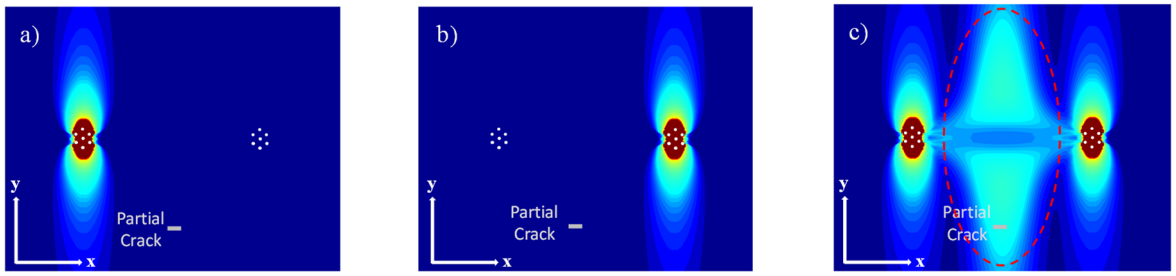

Figure 38. Three different sensor network arrangements and their estimated coverage area. a) left cluster. b) right cluster. c) both clusters.

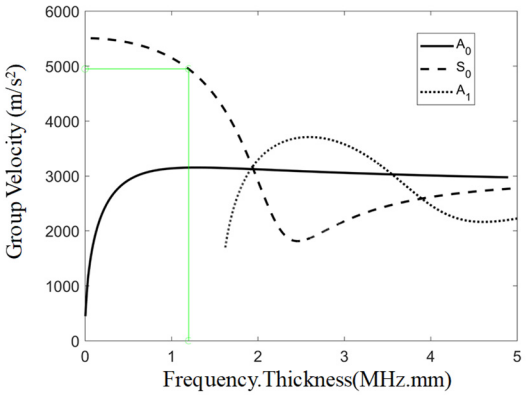

Figure 39. Lamb wave dispersion curves.

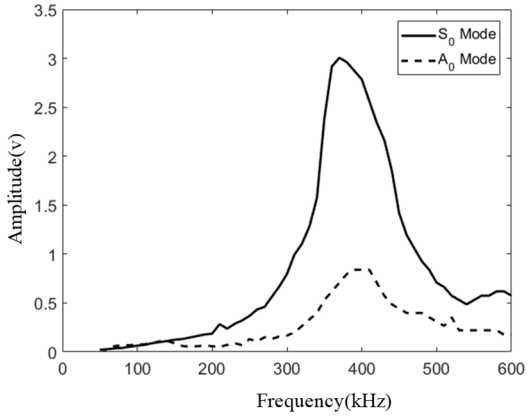

Figure 40. Tuning curves of S0 and A0 modes.

In the next step, S_0 and A_0 modes were isolated in acquired signals, and the pick amplitude in each mode for every frequency was determined using the maximum amplitude of the isolated packt determined by Hilbert Transform. At a frequency of 400 kHz, the amplitude of the fundamental symmetric mode is noticeably higher than that of the fundamental antisymmetric wave mode. Furthermore, at 400 kHz, the group velocities of S_0 and A_0 are substantially different, resulting in less interference of the multiple modes in the imaging stage. As illustrated in Figure 39, at this frequency, the velocity of the fundamental symmetric mode is about twice the velocity of the fundamental antisymmetric mode. This difference in velocities causes a preferable distance between two fundamental wave-mode packets in the transmitted signals that consequently makes it easier to detect A_0 and S_0 modes in the received signals. Additionally, this separation allows the imaging algorithm to be better adjusted to the complexities caused by many reflections created from the edges of the plate. It is also notable that at this frequency, other wave modes cannot propagate, making it easier to interpret the signals. Thus, in this study, a 400 kHz frequency was selected as the operational frequency.

The presence of a scatterer would cause the generation of an echo of the propagating wave that appears in the form of a spike in the stored signals. Hence, images visualizing the scatterers can be constructed by adding the signal values specifically selected for each pixel of the image. The image fusion method proposed by J. E. Michaels and T. E. Michaels [17] is adopted here and modified for a narrow-band excitation signal to visualize the crack. This method is based on back-scattered echoes due to defects and can be used to verify this paper's proposed coverage area estimation framework.

Assuming there is a scatterer at location (x, y), the time required for a wave to travel the total path between the transmitter and the scatterer and between the scatterer and the receiver can be calculated using equation (9) in which, x_t and y_t are coordinates of the transducer, x_r and y_r are coordinates of the receiver, c_g is the wave group velocity and i is a dummy index showing the specific transmitter/receiver pair.

$$T_i(x,y) = \frac{\sqrt{\left(x_{t_i} - x\right)^2 + \left(y_{t_i} - y\right)^2} + \sqrt{\left(x_{r_i} - x\right)^2 + \left(y_{r_i} - y\right)^2}}{c_g} \tag{9}$$

Each signal $s_i(t)$ is filtered (windowed) according to $T(x, y)$. The filtering function is shown in equation (10). ε in equation (8), is set to take into account any indeterminacy in selecting the group velocity value. Here $\varepsilon = 4\ \mu s$ is used in the imaging process. The group velocity used in the imaging procedure is obtained experimentally as 4650 m/s, and it closely matches the velocity of 4950 m/s obtained from the dispersion curve of S_0. As shown in equation (11), adding the maximum spike of filtered signals at each coordinate results in the pixel value at that location $E(x, y)$.

$$f(t) = \begin{cases} 1 \; if \; t - \varepsilon \leq t \leq t + \varepsilon \\ 0 \qquad\qquad otherwise \end{cases} \tag{10}$$

$$E(x,y) = \sum_{i=1}^{N_p} max\left(\left|s_i(t) f\left(T_i(x,y)\right)\right|\right) \tag{11}$$

Using only one signal (one pair) will result in an ellipse that shows the probable locations of scatterers. It should be noted that in our imaging, the reciprocity was ignored (e.g. both pairs of 1-2 and 2-1 sensor pairs are considered), and each sensor can act as both transmitter and receiver. As a result, in a network of N_s sensors, N_s^2 signals will be obtained. As the number of signals is increased, it is more likely that ellipses/circles would intersect at the location of the scatterer which causes increasing pixel intensity at the desired area. If only signals from defective parts are used in this scheme, resulting images would show not only desired scatterers, but also the structure's edges and artifacts from the signal first arrival. The latter is more of a problem if clusters of transducers are used, causing large artifacts to be produced in the space between clusters. This problem is solved by a pixel-wise subtraction of baseline images, resulting from signals obtained from an intact part.

Figure 41 illustrates the resulting map from all baseline signals. The horizontal and vertical edges of the plate are visible in Figure 41. The artifact in the middle is caused by the overlapping of the window width and the first arrival of the S_0 wave mode.

Figure 42 shows the results of the imaging procedure for data from the L cluster, the R cluster, both clusters without communication, and the imaging result when both clusters are working together (all 14 sensors are used in the imaging process). As was predicted by the coverage area estimated using the proposed framework, the critical crack is detected in Figure 42 (d) when clusters are communicating, while it was not detected in the other three cases.

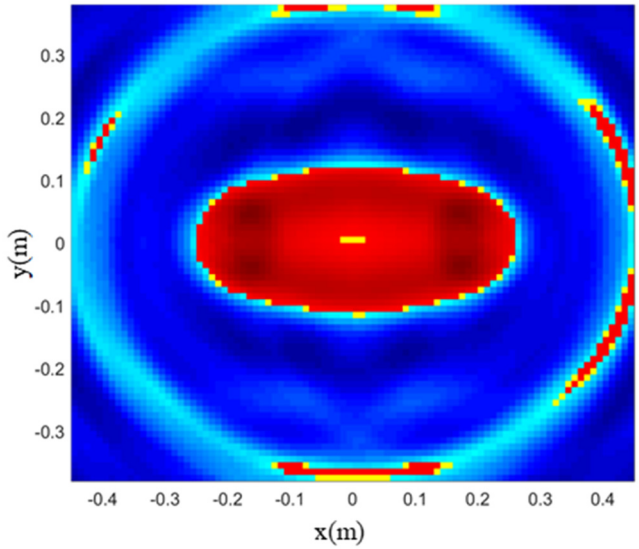

Figure 41. Baseline mapping.

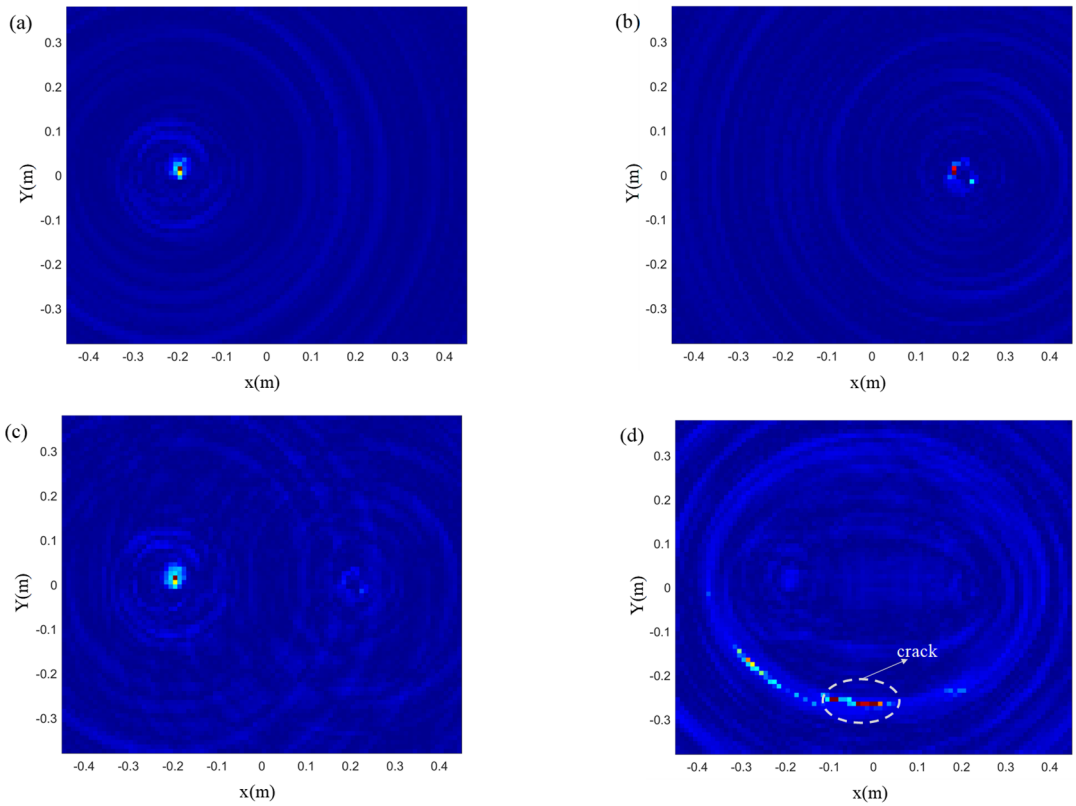

Figure 42. Results of crack detection procedure with different sensor arrangements. (a) L cluster. (b) R cluster. (c) L and R cluster without communication. (d) L and R clusters with communication.

Adding a new cluster helped to detect a crack that could not be detected with either of the clusters alone. This shows that the proposed framework accurately predicted the additional coverage area of the sensor network shown in Figure 38. The results in this section can be extended for two Quadruple configurations in the LTI grippers. While the imaging approach can help to localize the defects, it cannot be readily used for complex geometries such as joints and bends in the tubular components. In the following section, we proposed a deep-learning algorithm that can be used in more complex geometries.

1.3.2. Deep learning for defect detect

The EMAT was finalized and designed and fully integrated into the gripper of LTI in the previous section.

Data collection and labeling

Utilizing the design from Figure 43, raw time-series data was collected and stored. The data were collected for the a) intact pipe, b) pipe with corrosion, and c) pipe with a crack along with the corresponding signals that were generated (sample for pipe type). The data is pre-processed and labeled accordingly to the pipe classification. Two classifications are used for labeling during this study, cracks and corrosion are labeled with 0 and intact (no defect) data is labeled with 1. The univariate (amplitude) preprocessed dataset with labels has classes that are known in advance making it a supervised problem. The algorithms are trained on 75% of the full dataset and reshaped into an array of size (m, n, 1) using the NumPy library before training with the main objective to learn what distinctive features separate classes from each other. Where m is the number of samples (168) and n is the length of each sample (3002). 25% of the data is withheld from training and used for testing.

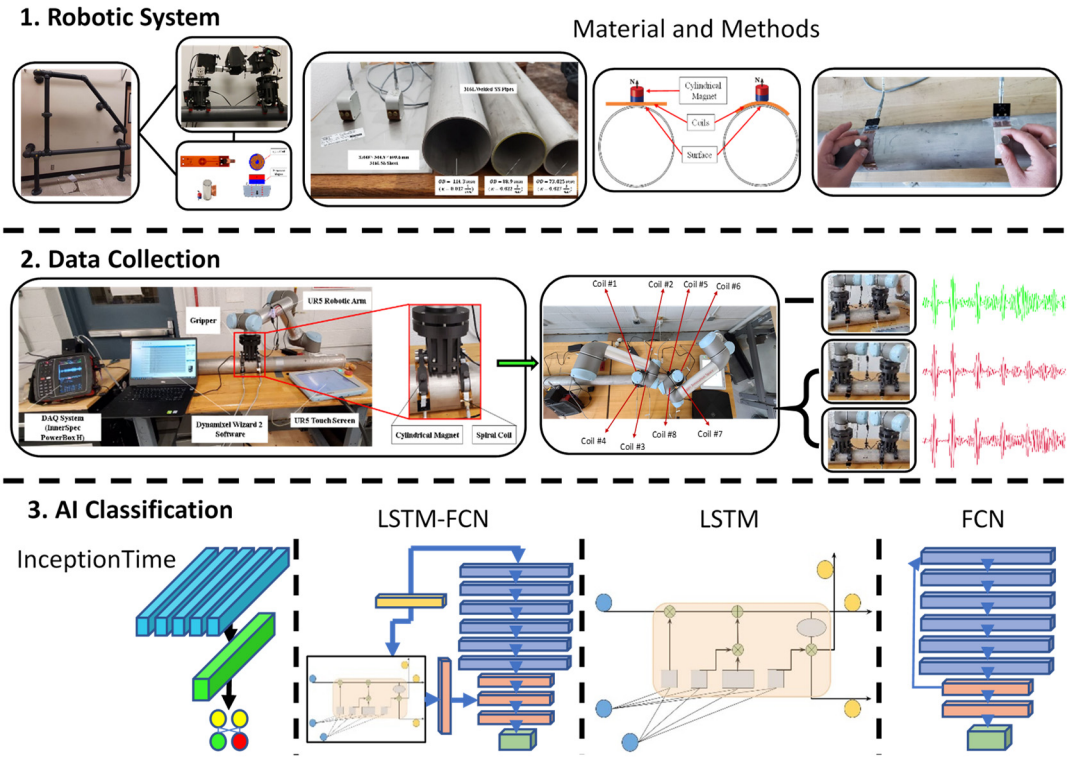

Figure 43. Flow diagram of complete DL-enabled robotic inspection investigation

1.4. Data Visualization and Exploration

Figure 44 displays an exhausting approach to exploring the autocorrelation of the time-series dataset. Lag observations are evaluated (Figure 44 a-c) and all samples are included for each of the three classifications and eight total previous observations (t-1 tot-8) are compared to observation at the next time step (t+1) in a scatter plot fashion. Position 1 (P1, intact position), shows the highest concentration of observations in a linear fashion, indicating the strongest

autocorrelation in the previous observation (t-1) to the next time step (t+1). As the time steps increase the relationship between the next observation decreases, as expected. This is useful knowledge when determining how many lags a user would like to implement into a classification model and for projecting out classifications (t+1…t+n). Position 2 (P2, corrosion) and position 3 (P3, notch defect) have similar correlation relationships between observations, however, are slightly weaker compared to position 1. For brevity, one sample for each classification output is visualized. Here, the autocorrelation (Figure 44 d-f) is explored for the first sample in the dataset which is coil 1 sending a signal to the receiving coil 2. Figure 44 visualizes 20 lags for each of the classifications with 95% confidence intervals shaded in blue. This validates the tabular results showing how the correlation of observation and another observation at a prior time step decreases to a point. At lag=t-6, the correlation becomes extremely weak. However, from lag=t-7 to lag=t-12 the correlation trends strongly in the negative direction then trends positively to lag=t-17. This appears to be a sinusoidal trend.

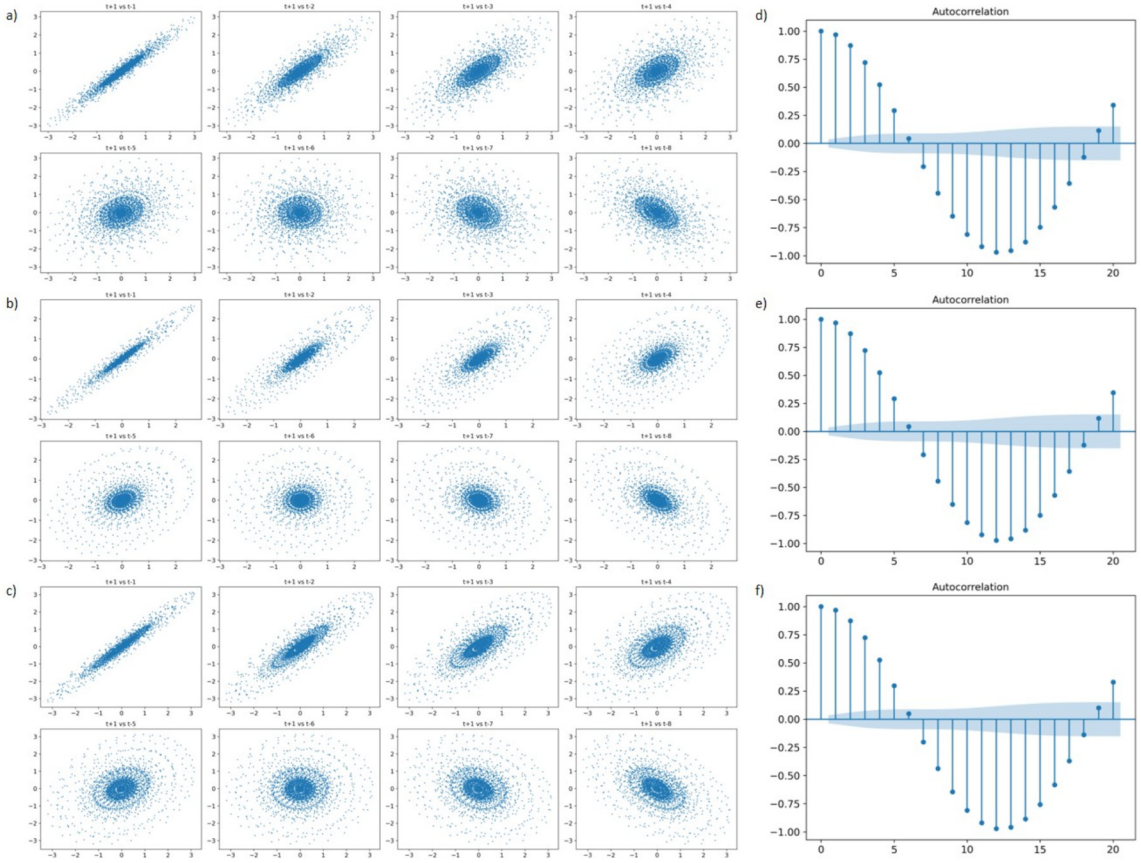

Figure 44. Lag observation plots for three classifications; a) P1, b) P2, and c) P3 and autocorrelation plots (lag=20) of the transaction between coil 1 to 2 of d) P1, e) P2, f) P3

The visual comparison of the two classes shows similar trends which may be problematic for model training. The classes do diverge around the 2000 index mark, suggesting that as time continues the signals differentiate from each other.

Violin plots were first introduced by Hintze and Nelson in 1997 (Hintze, 1998) and are an adaption of the box plot originally proposed by Tukey in 1977 [18]. The violin plot attempts to provide

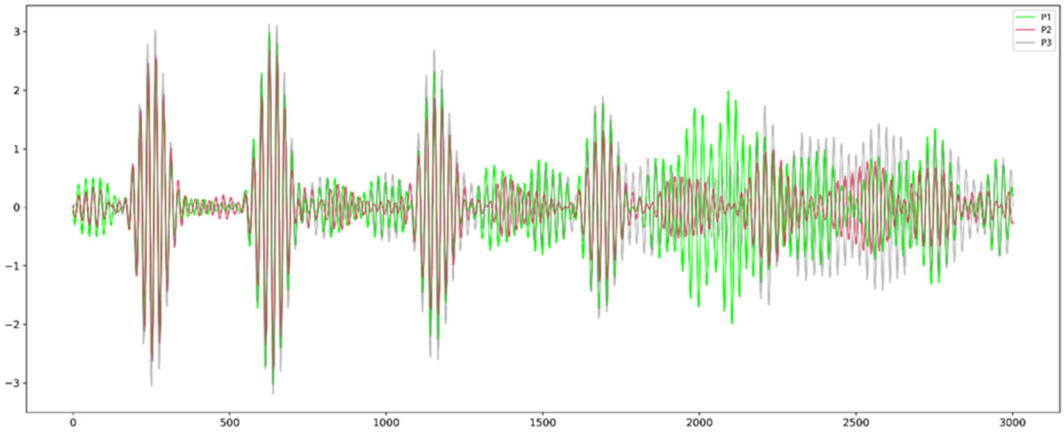

Figure 45. Time-series plot of no defect (P1), corrosion (P2), and notch defect (P3)

more insight into describing a dataset by combining information from a box plot and the density trace into a single graphical display [19]. Density traces work by graphically showcasing statistical distributional characteristics of batches of data as [19] :

$$d(x|h) = \frac{\sum_{i=1}^{n} \delta_i}{nh} \tag{12}$$

Where, the location density $d(x|h)$ at a particular point x is equal to the fraction of data values of n sample size, h interval width, and δ_i is a binary value (0,1). δ_i is one when the *i*th value is within the interval of $[x - \frac{h}{2}, x + \frac{n}{2}]$, and zero otherwise. For this study, violin plots are used as a visual representation to determine if there are any common trends in the time-series data depending on the class.

Figure 46, 5, and 6 dive deeper into the data analysis by visualizing the distribution of data points based on each different class. This tactic is useful for determining if there are any patterns that can be recognized as an initial step in determining if defects are present. The left column of Figure 46 highlights the violin plots for the distribution of data in line with the transmitting coil whereas the right column shows results from the signal as it coss the location of the defect. It can be seen that the data appears similarly distributed as transmitted by coil 1 in an inline fashion, received by coil 5 (Figure 46 c)) and coil 6 (Figure 46 e)) when compared to a cross-plane fashion, received by coil 8 (Figure 46 d)) and coil 7 (Figure 46 f)).

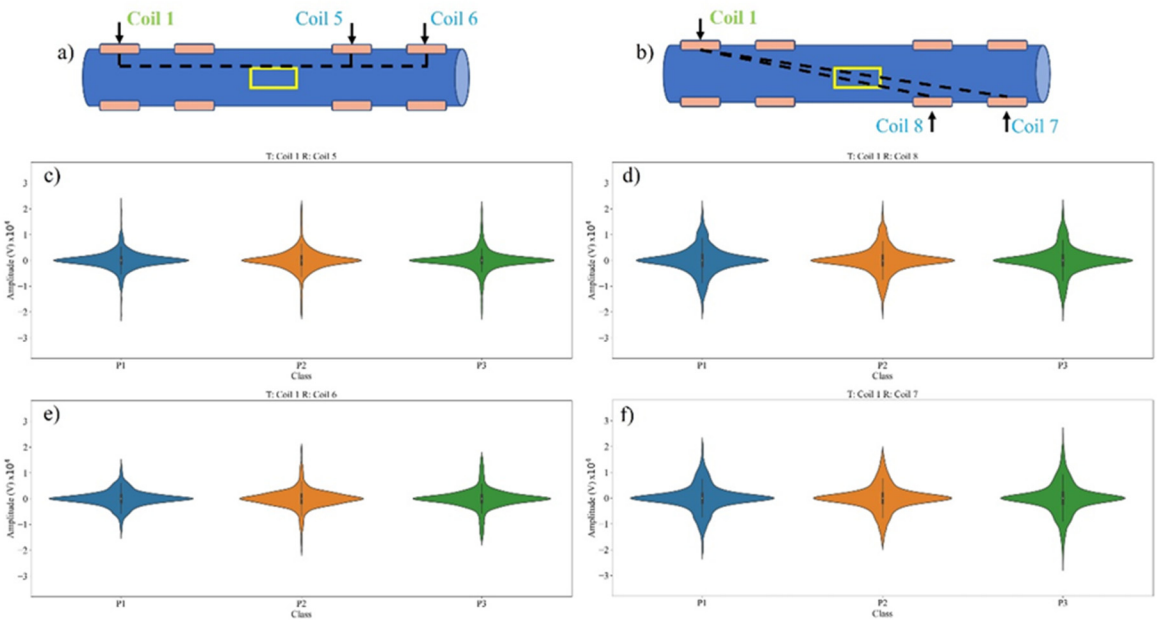

Figure 46. Violin plot of time-series distribution with no defects (blue), crack (orange), and corrosion (green) for transmitting coil 1 (a) schematic of inline arrangement, (b) schematic of cross-sectional arrangement, (c) receiving coil 5, (d) receiving coil 8, (e) receiving coil 6, and (f) receiving coil 7

1.5. Classification Results

After evaluating the time-series data we can see that within a certain limit, LSTM models are potentially the best solution from among the state-of-the-art DL techniques utilized in this investigation for time-series classification. For this model, the LSTM layer utilizes 100 memory units and the binary cross-entropy loss function. The LSTM model achieved an accuracy of 78.81% with a time-to-prediction of roughly 3 seconds. The next best model is the LSTM-FCN reaching an accuracy of 71.4% with roughly 1 second to classify the pipe condition.

Non-destructive evaluation (NDE) of two quality conditions of Stainless-Steel pipes was investigated for Time-series Classification (TSC) during the robotic inspection of structures using grippers of the LTI robot. This investigation explores the complex TSC problem as it pertains to the robotic inspection research sphere. A steady amount of algorithms exists for solving the TSC task, yet few have been tested on real-life tubular inspection scenarios. In an attempt to illuminate this problem, we have implanted and tested four Deep Learning (DL) algorithms designed for the TSC task and utilized them for classifying binary conditions of pipes during the robotic inspection. If a reliable DL network can be on-boarded to a robotic system, this method could provide useful knowledge and preventative advantage for Structural Health Monitoring (SHM) of physical components.
After visualizing and exploring the time-series dataset, it was apparent that prediction capabilities would be limited (forecasting and accuracy), and distinguishing between defects and

no defects would be difficult to classify. The LSTM model proposes the optimal solution for implementing an online solution to TSC tubular inspection. Since no physics-based model was used, this approach can potentially be used for more complex geometries of connections if the training data can be obtained. While this baseline DL performance is promising for implementation into tubular robotic inspection, however, sensor relationship to the algorithm should be further developed.

1.6. LTI robot navigation

The visual inspection of the pipeline was also considered in the LTI robot by integrating a distance high-resolution camera into the modular gripper of the LTI robot. While the visual inspection and image processing aspects were beyond the scope of the current research, the research team took the first step in the application of the camera for the navigation of the LTI robot. The navigation approach used in this research was based on integrating permanent indicators in the form of QR codes on pipelines to allow the LTI robot better be integrated into a digital twin concept for infrastructure inspection and maintenance. Initial programming of the vision data was completed. Several QR codes are printed and installed on the surface of the pipe used to validate the NDT aspects of the research. The UR5 arm shown in Figure 47 was used to move and locate the indicators to be able to place the gripper at the known positions.

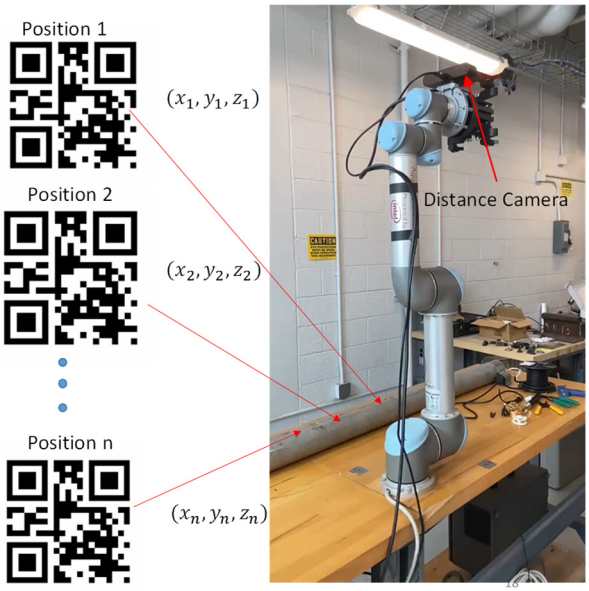

Figure 47. Integrated distance camera for robotic navigation

2. LTI robot

In this final report, we would like to briefly overview this entire journey over the past 4 years to develop the LTI robot. During this time, the LTI robot has transitioned from an initial conceptual design to the first completely assembled robot and finally the optimized robot, described in the following sections.

One of the crucial components of the LTI robot is the lizard-inspired frictional pads that allow the robot to easily attach and detach itself from the rough exterior of a coal power plant boiler tube. To characterize and optimize the design of these frictional pads we designed a cartesian robot to test the frictional properties of these pads, as described in the following section.

2.1. Optimized frictional setup design

The frictional setup designed to test the gripper pads was based on a simple 3-axis cartesian system with a linear actuator attached to the XY plane (Figure 48 TL). This first version was designed for high-precision measurements at small normal loads implemented on flat pads/surfaces. However, we needed to redesign this friction setup to accommodate larger normal forces applied on curved surfaces (Figure 48 TR). In the second version of the friction setup, we used a 6-axis force sensor rated to measure forces up to 20 kN with an accuracy of ± 0.5 N. Nonetheless, during our tests with this setup, it was found that friction measurements under normal loading conditions higher than 35 N were not consistent/reliable. To test under higher normal loading conditions, we had to reinforce the XY plane by adding a parallel support system to the existing XY plane. We also replaced the current DC motors, rated at 2.94 Nm stall torque to motors with a 57.27 Nm thereby increasing the torque on these individual axes by approximately 20 times the initial value (Figure 48B). Replacing the motors required replacing the motor drivers as well to be able to handle higher operating currents. For our application, it was found that Pololu Dual G2 High-Power Motor Driver 18v22, was the best choice. This motor driver is a MOSFET-based motor driver which can handle operating currents up to 30 A per channel, unlike the previous motor drivers which could withstand 12 A per channel under continuous operation. We designed a custom motor driver shield as seen in Figure 49 to connect the controller with the motor driver with the help of a fixed connection to prevent any signal losses and any noise caused due to wire-wire connections between the motor driver and the controller. This printed circuit board would interface with different motor drivers and control the individual axis as well as provide over-current protection to the overall circuit.

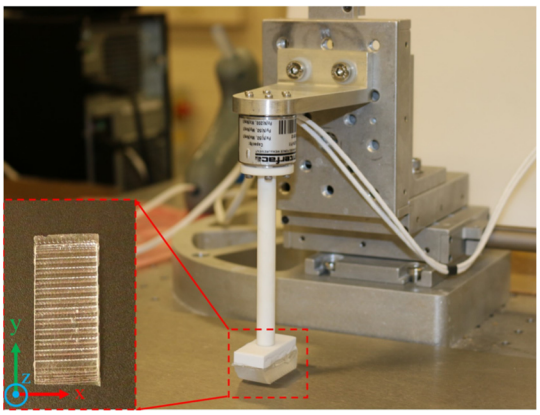

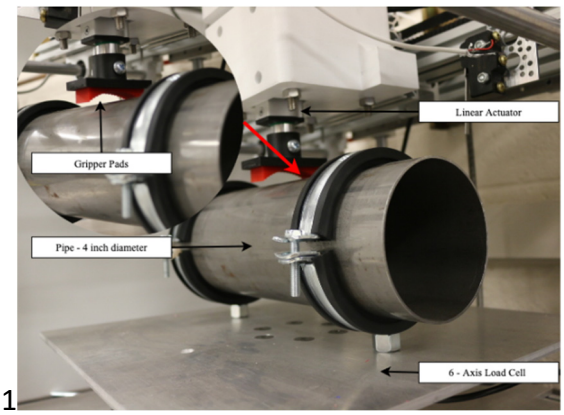

1

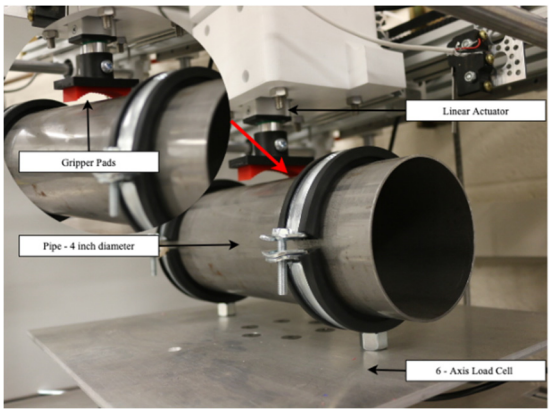

Figure 48. (Top Left) The initial friction setup used to test the friction pads. (Top Right) Modified friction setup to test flat back gripper pads under higher loading conditions in Z - Axis. (Bottom) Optimized friction setup used to test the curved friction pad pads under higher normal loads in X and Y Axes.

With these motor drivers, we would be able to hold the motors in place under high torque conditions as well as increase the loading force values beyond 35 N. With these modifications to the test setup, we wish to perform more tests with the gripper pads that would help us to optimize the design for higher normal forces in the X and Y directions.

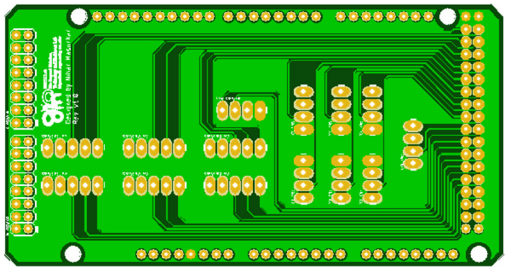

Figure 49. Printed circuit board (PCB) designed for the friction setup controller

2.2. Conceptual Design of the LTI robot

The first conceptual design was comprised of two grippers separated by two linear actuators to allow the robot to move along the length of the boiler tube. The two rotational components at the grippers allowed the robot to perform complex motions such as moving along the bends of the boiler tube as shown in Figure 50.

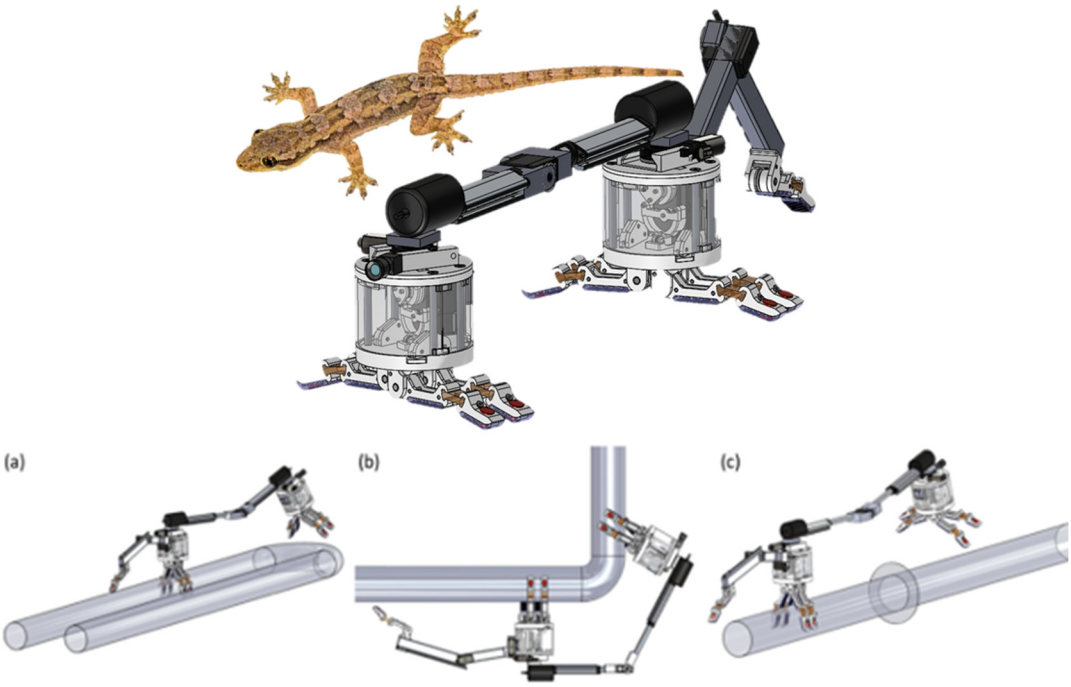

Figure 50. Conceptual design of the Lizard Inspired Tube Inspection Robot.

2.3. Frictional Pads and Gripper Fingers

2.3.1. Finger Design 1

The first finger design had a few key aspects that differentiate it from the second iteration. The first is the location for the housing of the EMAT sensor, which was located in the center of the finger, directly underneath the friction pad. The second notable feature was the shape of the friction pad. The friction pad was flat on the side that connected to the finger and had ridges on the curved side, as can be seen in Figure 51. This was meant to match the curve of the pipe and have a smaller arc length, so the fingers didn't need to have full access to the pipe. The third feature was the material of the friction pad themselves. The finger pads were originally made with Polydimethylsiloxane (PDMS), as it proved to provide a substantial amount of frictional force. The PDMS used was Dow and Corning's Sylgard 184 in a mixing ratio of A:B being 10:1. This material, being semi-elastic, allowed for the pad to semi-expand along the surface of the pipe, and ensured that the entire pad made contact with the pipe and the maximum amount of friction was achieved.

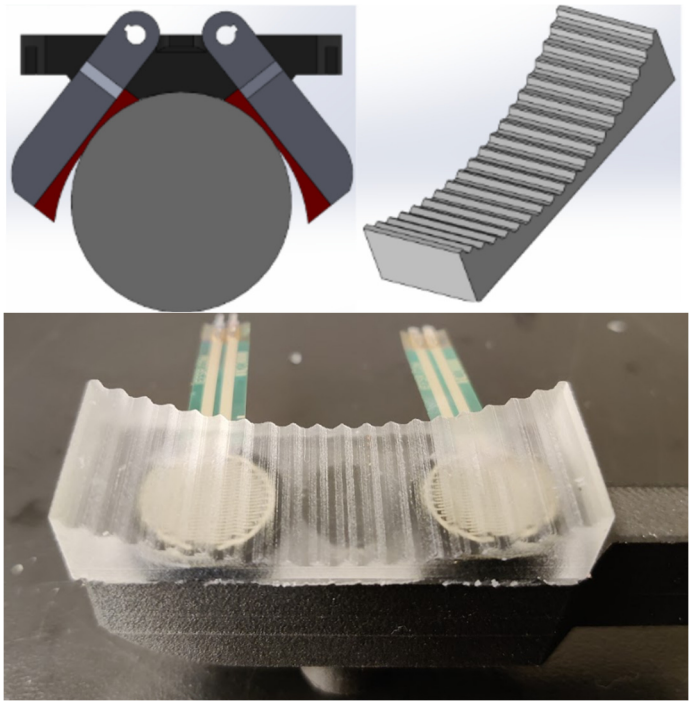

Figure 51. The first finger design with flat back frictional gripper pads.

2.3.2. Finger Design 2

The initial finger design worked fairly well; however, it could not exert enough force to keep the robot against the pipe. The second design solved this issue by extending the finger length, housing the friction pad, and having a curve to match the pipe, as seen in Figure 52. In addition to changing the finger shape and the friction pad shapes, the material was changed to a synthetic silicone polymer, as it proved to better grip surfaces and be more durable than the PDMS pads. Finally, the EMAT sensor was placed on the side of the finger, as that would allow for easier access to the sensor without having to take the friction pad off (Figure 53).

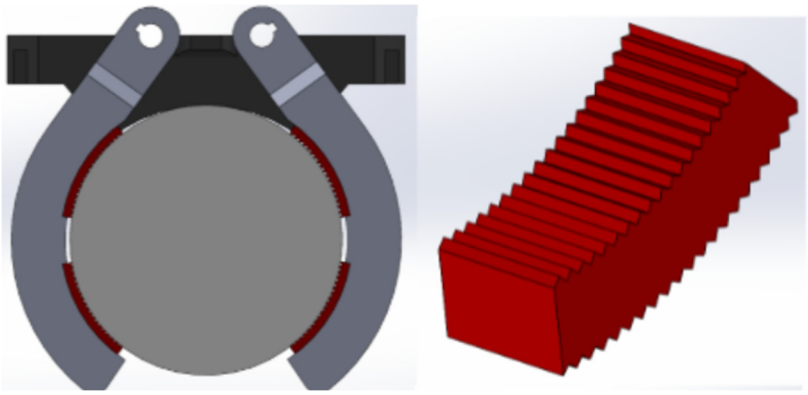

Figure 52. The second design for both the fingers as well as the friction pads.

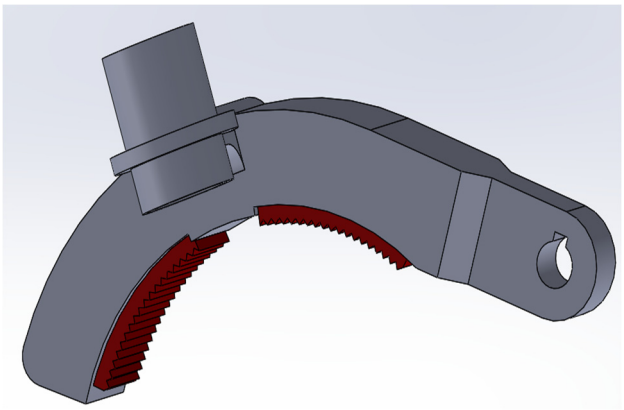

Figure 53. The two different finger designs. (Left - first design with the EMAT housing placed on the side. Right - new curved finger design).

2.4. Gripper

2.4.1. Gripper Design 1

The initial gripper design was inspired by Yale's OpenHand Project which utilized kevlar strings to actuate the fingers. There were 3 different strings tested, 2, 4, and 8 fold. The 8-fold proved to be the best for the application as the other two would snap under the load applied. Overall, the kevlar string proved to be problematic in several regards. Namely, it was difficult to construct and maintain, and it broke frequently. It also struggled to maintain tension in the string after multiple actuations, meaning that it would not be reliable in a field application. The constructed prototype is shown in Figure 54.

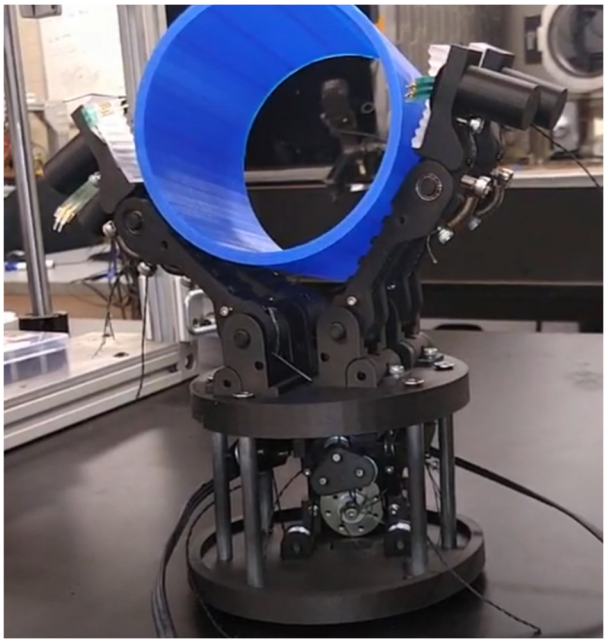

Figure 54. The first gripper design with the kevlar strings connected to the fingers.

2.4.2. Gripper Design 2

The second gripper design utilized a worm gear and wheel to close the fingers and as shown in Figure 55. This allowed for easier construction and maintenance and improved durability. This change also increased the force that could be put into gripping the pipe without the risk of the fingers opening. The gear ratio between the worm gear and worm wheel is 20:1, as the torque output is the priority in order to maintain the friction between the robot and the pipe.

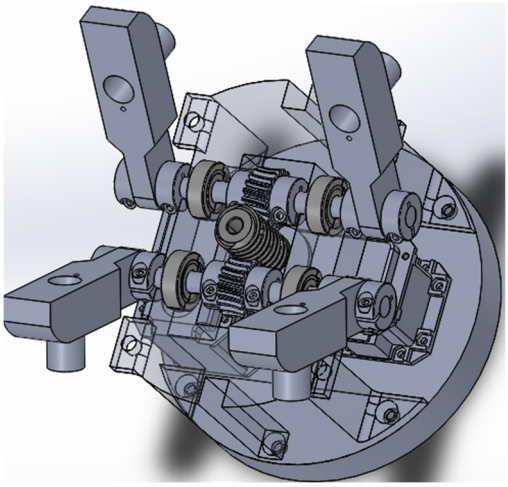

Figure 55. The second gripper design utilizes a worm gear and wheel to open and close the fingers.

2.4.3. Gripper Comparison

The second gripper design has proven to be sturdier, stronger, and more reliable than the initial design. The kevlar strings tended to stretch over time, or break during use, while with the newer gripper, the gears do not have any of these issues. The only issue that persists is that the fingers tend to bend slightly when the robot is gripping the pipe via one gripper.

2.5. Gearbox B

2.5.1. Gearbox B Design 1

The first gearbox B design utilized a U-Bracket and worm gears to change the angle of the grippers, depicted in Figure 56. The original ratio for the worm gear and wheel was 1:10, as the initial torque needed in gearbox B was calculated to be 8.5 Nm with a factor of safety of 10. The U-Bracket acting as the joint between a gripper and gearbox b, was changed because it was observed that the U-Bracket bent along the side during actuation and made the structure weak at that point.

Figure 56. The front and back side of the U-bracket in the first design of gearbox B.

2.5.2. Gearbox B Design 2

The second design of gearbox B replaced the U-Bracket in design one with a custom triangular piece. The design still utilized the 10:1 worm gear and wheel to allow the gripper to be angled. This change is illustrated in Figure 57. With this design, the working angles for the gearbox was roughly 105 degrees, starting with the gripper being in line with the actuators to just slightly past perpendicular to them.

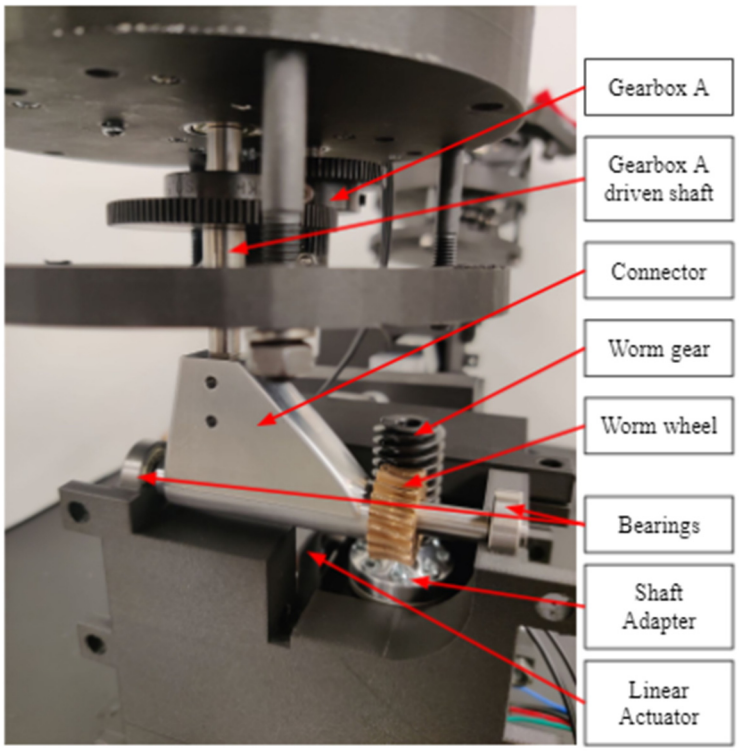

Figure 57. The second design of gearbox B.

This design proved to work better than the previous one, however, the joint connecting to the gripper was fairly thin, decreasing the factor of safety (as discussed in section 2.11.1). Thus, the design of gearbox B needed to be changed once more.

2.5.3. Gearbox B Design 3

Gearbox B design was changed to allow for a more stable connection between this gearbox and the gripper, as well as to allow a higher degree of rotational freedom for the gripper (Figure 58). Since the 2nd LTI robot prototype is no longer using linear actuators but rather rotational actuators, gearbox B had to also work in tandem with gearbox C. This was done similarly to previous designs with a worm gear and wheel, with the exception that they rotate a shaft that is fixed to a connecting arm. This allows for the gripper to rotate around that shaft, meaning that it can work in tandem with gearbox C to achieve linear motion or rotate separately in pursuing another action. The entire weight of the Gearbox B assembly is roughly 570 grams. It has a height of 146.5 mm, from the motor to the top of the gearbox housing, a length of 168.47 mm, and a width of 107 mm. This has been a size reduction of around 20% with respect to weight and size. The new gearbox B can also rotate up to an angle of 130 degrees, starting with the links parallel with the worm gear shaft to the contact of the standoff with the gearbox B motor.

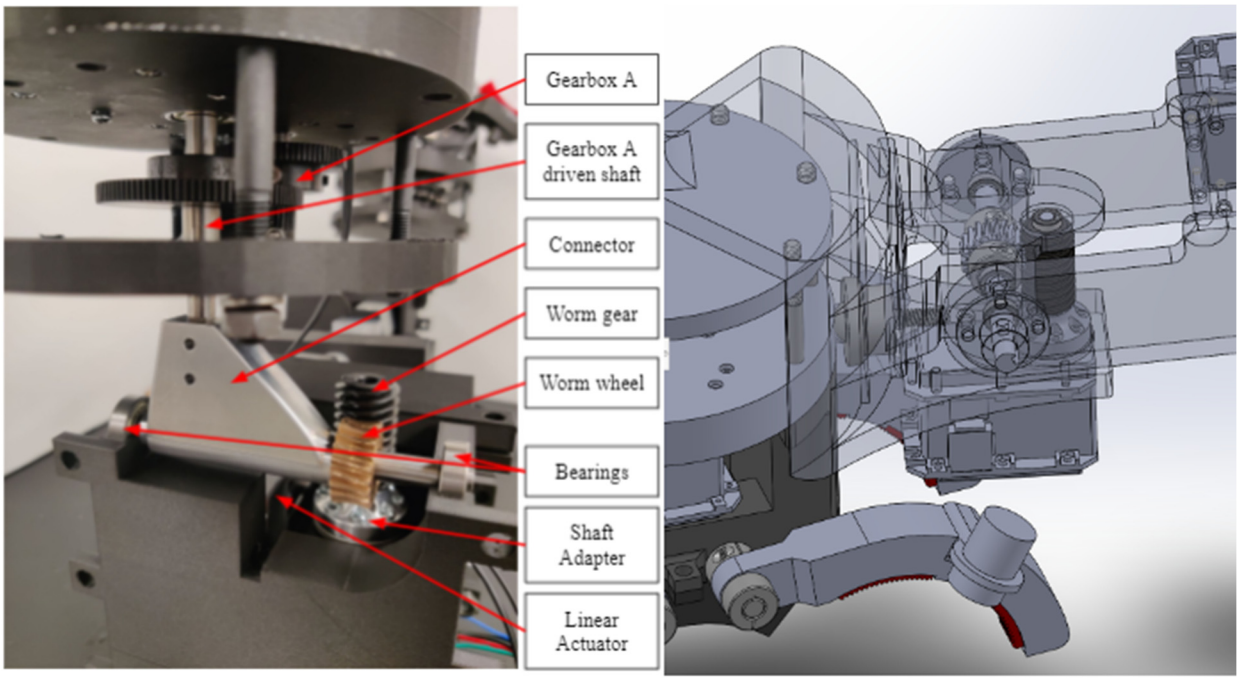

Figure 58. Gearbox B comparison (Left - Design 2, Right - Design 3).

2.6. Gearbox C

2.6.1. Gearbox C Design 1

The first gearbox C design was technically composed of several parts: two linear actuators that expanded and contracted to provide linear motion and a gearbox assembly that controlled the angle between the two actuators. This design proved to be bulky, heavy, and slow. The linear actuators weighed significantly relative to the rest of the robot, at roughly 1kg per actuator. Along with that, the height that the linear actuators were at also caused high stress during different configurations, such as vertical or upside down. Ultimately, the design needed to be faster, smaller, lighter, and overall more sturdy.

2.6.2. Gearbox C Design 2

For the optimized version of gearbox C, we designed a scissor-like mechanism to increase the distance between the two grippers on both ends of the mechanism (Figure 59). We designed two arms that are actuated by a gearbox assembly in between that can pull the grippers closer to each other and push them apart to vary the linear distance. Since this design relies on the two links that can pull-push the grippers together, we can vary the length of our application making it a very modular design. The new gearbox C has a height of 60 mm and a maximum width of 157 mm from the motor to the shaft end. It also has a minimum length of 320 mm and weighs around 860 grams. This change will result in speed improvements and will lighten the robot significantly.

This means that the weight is concentrated in the grippers rather than the center. It also means that during the linear motion, the weight will remain closer to the pipe.

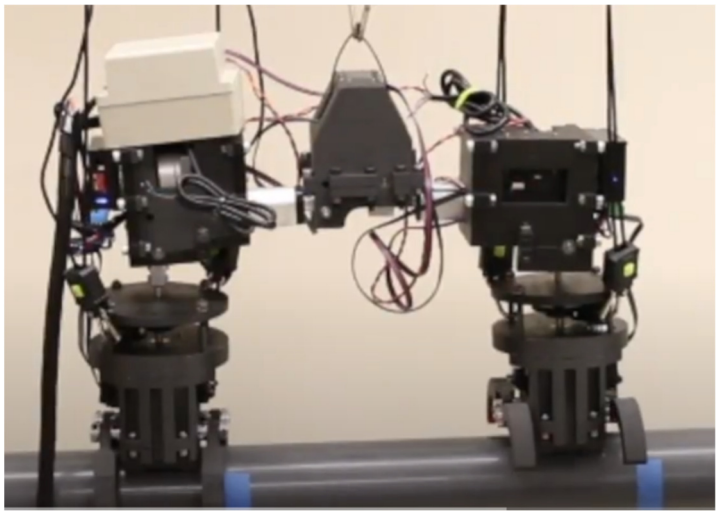

Figure 59. Gearbox C comparison (Left - Design 1, Right - Design 2).

2.7. Controller Board

For controlling the robot, we first started with a simple PID controller for the Dynamixel motors which set the individual motions for every single actuator on the LTI robot. There were two simple H-Bridge drivers as well to control the linear actuators in the first prototype of the LTI robot. As we transitioned to the optimized design, where we replaced the linear actuators with dynamixel motors that would work synchronously, we switched from a U2D2 controller board to a new board from Robotis; OpenRB-150 as seen in Figure 60.

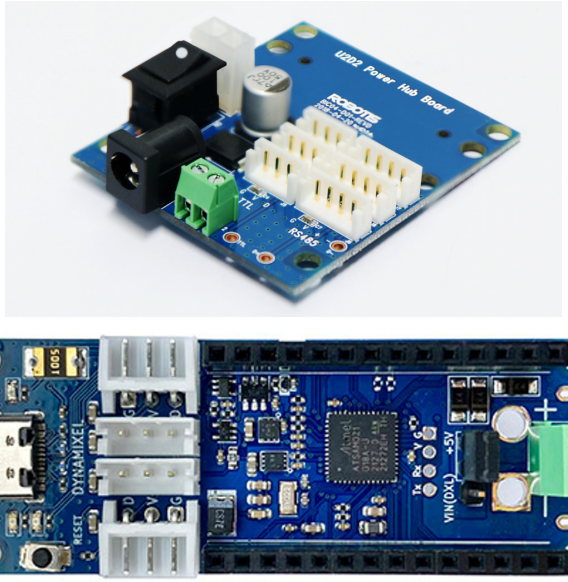

Figure 60. (Top) U2D2 Controller board used for controlling the first prototype of LTI Robot. (Bottom) OpenRB-150 used to synchronize the Dynamixel motors in the optimized design.

2.8. First Prototype of LTI Robot (Mk1)

Based on the above description of the various gearbox and gripper modifications, we were able to assemble the second design of the LTI robot. We integrated Finger Design 1 with Gripper Design 2. To lift the gripper away from the boiler tube, we used Gearbox B Design 2 and for moving the robot along a single line, we used Gearbox C Design 1 as mentioned above. The complete assembly, dimensions, and kinematic tree of the first LTI robot prototype can be seen in Figure 61-Figure 63.

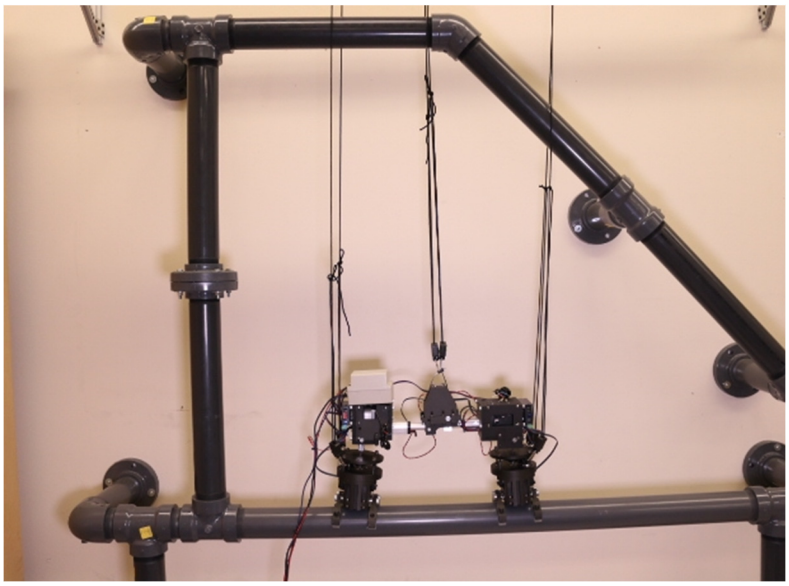

Figure 61. The first prototype of LTI Robot (Mk1) was completely assembled and ready for testing.

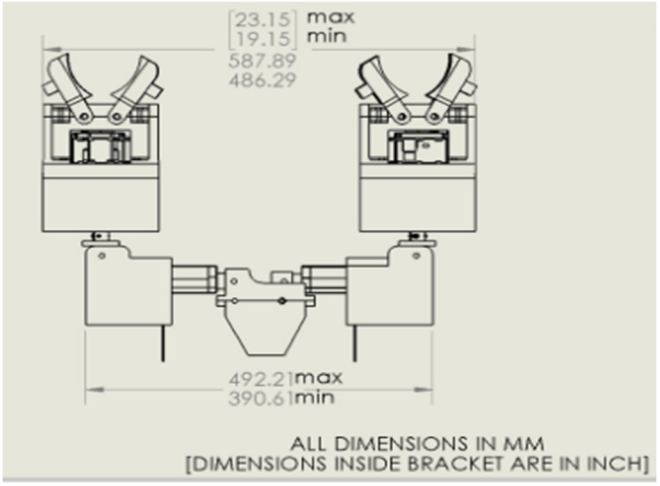

Figure 62. The minimum and maximum dimensions of the first prototype.

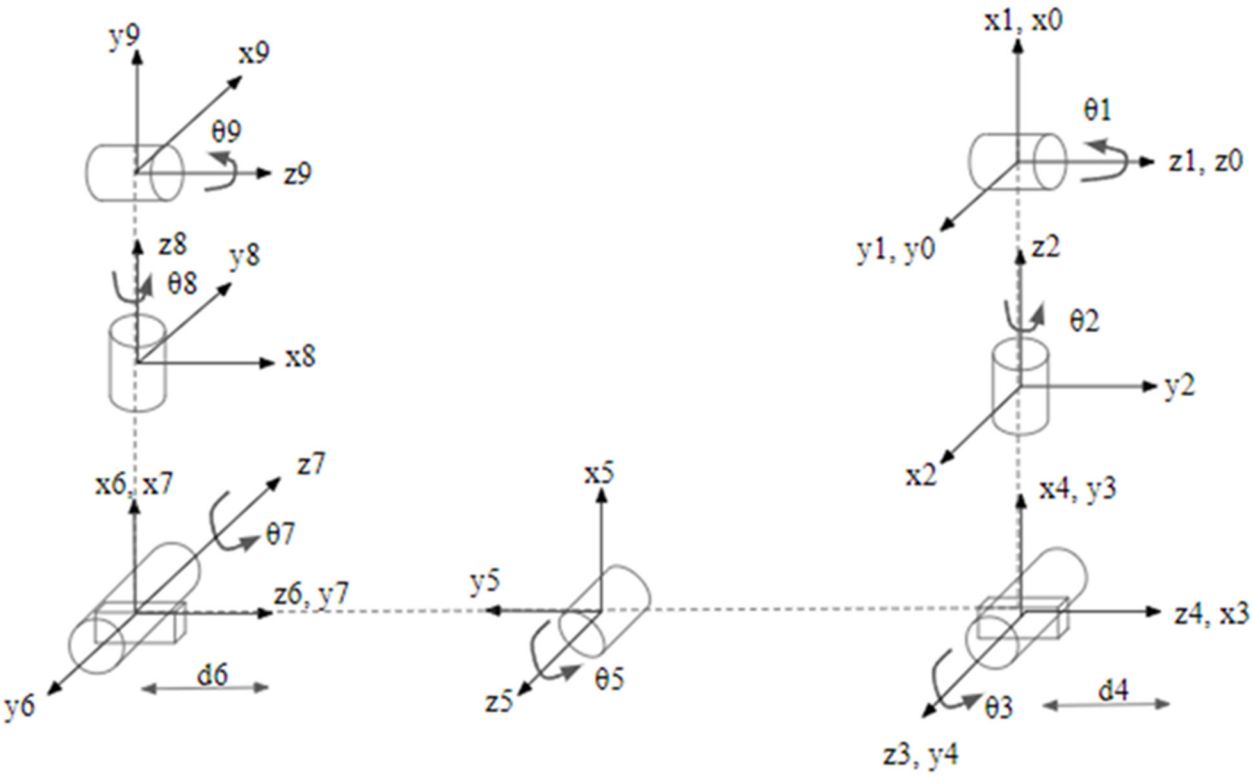

Figure 63. kinematic tree of the first LTI robot prototype.

2.9. Second Prototype of LTI Robot (Mk2)

Based on the mobility tests performed on the test setup (Figure 61), we came to the conclusion that to improve the mobility of the LTI robot the overall weight of the robot needs to be reduced. In order to do so, we analyzed the overall design and calculated the weight of every individual component of the robot. It was found that the heaviest part of the design was the linear actuators separating the two grippers whose weight came to around 1 kg per linear actuator. In order to replace them, we had to re-design gearbox C and gearbox B to remove the linear actuators and replace them with a similar joint that would be able to perform the same level of movement. We were also able to simplify the robot while maintaining the same degree of movement as in the previous designs. In this report, we will discuss the different changes made to the LTI Robot to improve mobility while reducing its size/weight.

2.10. Design Comparison

The first prototype, although it illustrated the basic movements and abilities that the robot was designed to complete, is outclassed by the second prototype in terms of speed, size, and mass. With this overall new improved design, we reduced the overall weight from 7 kg to 5.65 kg and at the same time retained the same level of mobility in terms of all degrees of freedom. With the improved design, we were able to control the robot to maximize the reach of the grippers and provide sturdy movement. The second prototype also met the proposed goals for design

optimization, as it is roughly 1.35 kg lighter than the previous iteration, 140 mm shorter in height, and able to achieve the maneuvers. The fully extended length of the second prototype is 620 mm. There is, however, one area where the second prototype falls behind the first prototype, which is in its compressed state. The first prototype could compress to a length of 486 mm while the second prototype can only compress to a length of 515 mm. Another way that the second prototype improved upon the design of the first was in the rotational freedom granted through gearbox B. The first prototype had a working angle range of 105 degrees, while the second has a working angle of 130 degrees, roughly a 23.8% increase in mobility. Table 6 provides a detail comparison of the two LTI robot prototypes.

Table 6. Performance parameters of the first prototype and the second prototype.

Parameters	First Prototype	Second Prototype
Maximum Torque on fingers @ 12V (Nm)	84 Nm	168 Nm
Gripper Gear Ratio	1:10	1:20
Gearbox A	1:21	1:21
Gearbox B	1:10	1:20
Gearbox C	1:10	1:21
Weight (kg)	7 Kg	5.65 Kg
Height (mm)	335.55 mm	195.82 mm
Compressed Length (mm)	486.29 mm	515.80 mm
Extended Length (mm)	587.89 mm	620.18 mm
Width (mm)	152.30 mm	159.30 mm
Single Cycle Travel Distance (mm)	101.6 mm	104.38 mm
Max Linear Speed (Theoretical) (mm/s)	5.6 mm/s	17 mm/s
GBB Joint Range (degrees)	105°	130°
GBC Joint Range (degrees)	45°	110°

2.11. Performance Evaluation

In this section, we will present and discuss the results of the robot structural analysis and friction pad characterization.

2.11.1. Structural evaluation using finite element analysis (FEA)

Detailed structural analysis of the first LTI robot prototype has been performed using the FEA feature of SOLIDWORKS© software. Simulations have been performed for multiple orientations and combinations of joint angles of the robot. The parameters such as a factor of safety (FOS) and stress were studied to determine the structurally weak points of the robot. Some of the critical configurations in which the robot components experience extreme loading and the simulation results for those are discussed in the following.

Orientation 1 shown in Figure 64 is one of the critical orientations that produced a lower FOS. In this orientation, one of the grippers holds onto a horizontal pipe, and the rest of the body hangs vertically downwards. It is not a common position or orientation that the LTI robot will experience, however, it is a possible configuration when the robot transitions between two horizontal pipes. As shown in Figure 64, the robot has the lowest structural FOS of 2.487 at the gearbox A driven shaft.

In orientation 2, illustrated in Figure 65, one of the grippers holds onto a vertical pipe and the rest of the body hangs vertically downwards perpendicular to the gripper. This particular orientation may be experienced when the robot is climbing vertically upwards. As shown in Figure 65, the maximum stress acts on the gearbox A driven shaft. The FOS at this point in the shaft was found to be 1.793 and thus, the robot can still structurally survive such a maneuver.

In addition to the static strength testing of the whole body, FEA was performed on the gripper to find the minimum FOS of the finger at the maximum torque applied by the Dynamixel motor (8.4 Nm). The lowest FOS in this simulation was 3.4 at the finger.

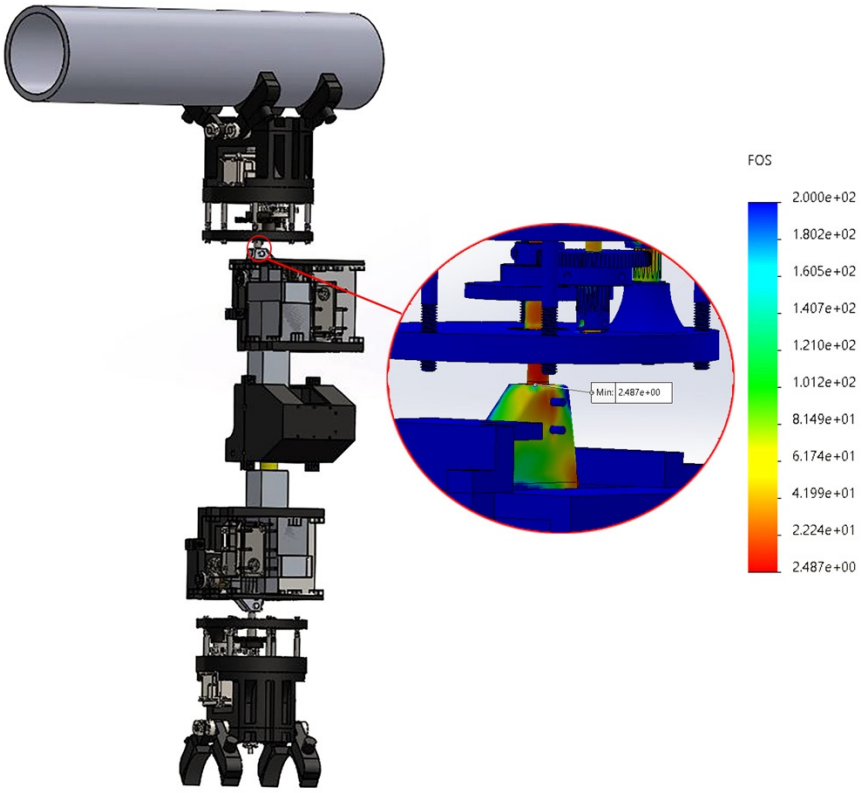

Figure 64. Orientation 1 and the FEA result at its weakest point.

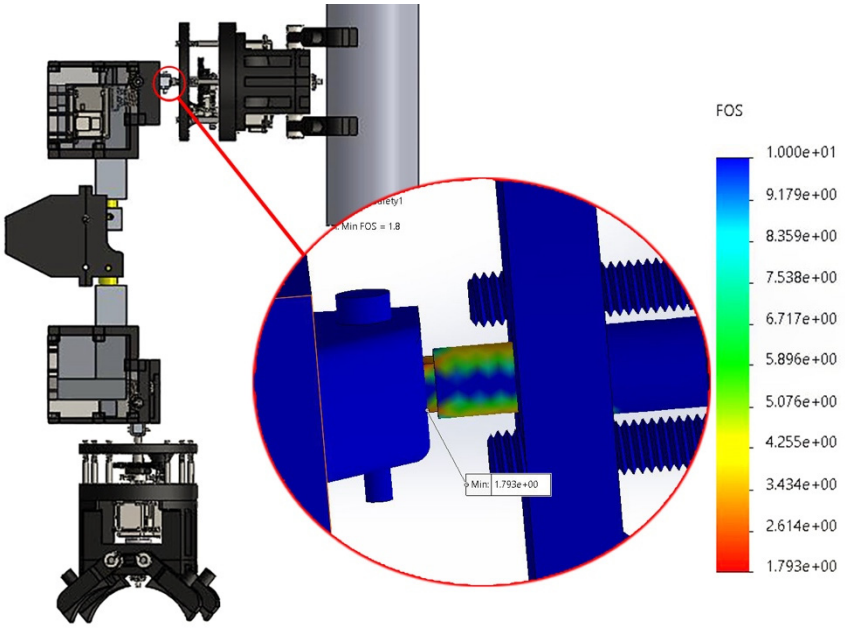

Figure 65. Orientation 2 and the FEA result at its weakest point.

2.11.2. Gripper Pad Characterization

We measured the frictional properties of two different designs of friction pads (Figure 51 and Figure 52) made of PDMS with silicone pigment. However, material and design optimization of the friction pads are beyond the scope of this study and are part of future work.

To perform the friction tests, we used the setup illustrated in Figure 48b. We mounted the pads on the bottom of the linear actuator and pushed the pad down onto a curved surface of a tube. For this test, the tube was attached to a 6-axis force sensor, Interface ForceTM 6A68E-F11. The force sensor was rated to measure forces up to 20 kN with an accuracy of ± 0.5 N.

For this test, we particularly recorded the change of forces in the normal (Z) and shear (Y) directions over time using an Interface ForceTM BX8 data acquisition (DAQ) system. Three pads were fabricated for each of the two designs shown in Figure 51 and Figure 52 and three tests were performed on each pad using the same testing procedure. For this test, we applied a normal load of 30 N along the Z axis. Once this load was achieved, the setup paused for 15 seconds, the Z-axis actuator was locked in place and the pad was then slid along the length of the attached tube (Y-axis). This sliding was done over a distance of 100 mm at the speed of $5 mms^{-1}$. These testing parameters were estimated based on the operational condition of the robot.

The mean static friction coefficient of the flat back and curved pads were around 0.49 ± 0.01, and 0.54 ± 0.01, respectively (Figure 66). The maximum normal load available on each finger is 30.24/(4*0.04) = 189 N. Thus, considering the friction coefficient of 0.49 and 0.54 for flat and curved pads, the maximum available shear load on each finger becomes 0.49 * 189 = 92.61 N and 0.54 * 189 = 102.06 N, providing a FOS of 10.8 and 11.9, respectively to support the robot weight.

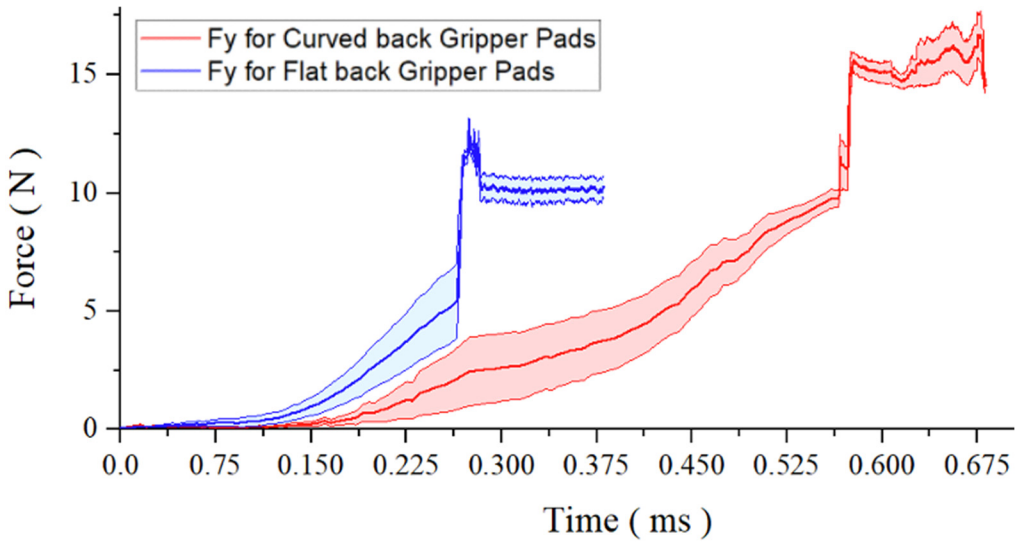

Figure 66. Normal and shear forces versus time.

3. Dissemination

Journal publications

1. H. Nemati, F. Alvidrez, A. Das, N. Masurkar, M. Rudraboina, H. Marvi, and E. Dehghan-Niri, "Integrating electromagnetic acoustic transducers in a modular robotic gripper for inspecting tubular components" Materials Evaluation, pp. 715-727, 2021 [4]
2. M. Ghyabi, H. Nemati and E. Dehghan-Niri, "*A simplified framework for prediction of sensor network coverage in real-time structural health monitoring of plate-like structures*," Structural Health Monitoring: an International Journal, 2021 [11]
3. S. Zamen, E. Dehghan-Niri, M. Ilami, V. Anand Senthilkumar, and H. Marvi, "Recurrence analysis of friction based dry-couplant ultrasonic Lamb waves in plate-like structures", Ultrasonics, Vol. 120, March 2022, 106635 [10].
4. Das, M. Rudraboina, N. Masurkar, F. Alvidrez*, E. Dehghan-Niri, and H. Marvi, "Lizard Inspired Tube Inspection Robot", International Journal of Intelligent Robotics and Applications, under review.
5. S. Hespeler, N. Masurkar, H. Marvi, and E. Dehghan-Niri," Robotic enabled non-destructive testing of pipelines using deep learning data-driven models", in preparation
6. N. Masurkar, V. Anand Senthilkumar, E. Dehghan-Niri, and H. Marvi "Novel friction-based robotic platform for pipeline inspection", in preparation.

Thesis

1. F. Alvidrez, "*INTEGRATING ELECTROMAGNETIC ACOUSTIC TRANSDUCERS IN A MODULAR ROBOTIC GRIPPER FOR INSPECTING TUBULAR COMPONENTS"*, NMSU, 2021.
2. N. Masurkar, "*Design and Control of a Lizard-inspired Tube Inspector Robot"*, ASU, 2022.

Patent

1. H. Marvi, E. Dehghan-Niri, and M. Ilami, "*Systems and methods for a Lizard-Inspired Tube Inspector (LTI) robot"*, US patent, 11,504,854, 2022 [20].

Conferences

1. Ghyabi and E. Dehghan-Niri, "*Structural health monitoring of metallic plate-like structures for partial crack detection"*, ASNT 28th Research Symposium, Hyatt Regency Orange County Garden Grove, CA, April 1-4, 2019.
2. Ghyabi and E. Dehghan-Niri, "Comparison of Coverage Areas of Two Different Sensor Network Arrangements for Structural Health Monitoring of Plate-Like Structures", SPIE Smart Structures + Nondestructive Evaluation, Denver, CO, 3-7 March, 2019.
3. S. Zamen, M. Ilami, V. Senthilkumar, H. Marvi, and E. Dehghan-Niri, "Experimental Evaluation of Friction Effects on Lamb Waves Generation", ASNT Annual Conference, Virtual, Nov. 2020.

4. H. Nemati, M. Ilami, J. Bhadra, H. Marvi, and E. Dehghan-Niri, "Evaluation of curvature effects on the performance of an integrated robotic gripper equipped with electromagnetic acoustic transducers", ASNT Annual Conference, Virtual, Nov. 2020.
5. H. Nemati, F. Alvidrez, A. Das, N. Masurkar, M. Rudraboina, H. Marvi and E. Dehghan-Niri, "Toward Automated Ultrasonic Inspection of Pipelines and Tubular Components" ASNT Research Symposium, Virtual, March 2021

The PI of this project was the guest editor for the special issue related to robotic inspection in the Materials Evaluation journal. This special issue open access journal covers 3 projects funded by NETL.

1. H. Nematia, F. Alvidrez, A. Das, N. Masurkar, M. Rudraboina, **H. Marvi**, and **E. Dehghan-Niri**, "Integrating electromagnetic acoustic transducers in a modular robotic gripper for inspecting tubular components" Materials Evaluation, July 2021,

2. C. Lara, J. Villamil, A. Abrahao, A. Aravelli, G. Daldegan, S. Sarker, D. Martinez, **D. McDaniel**, "Development of an Innovative Inspection Tool for Superheater Tubes in Fossil Energy Power Plants" Materials Evaluation, July 2021,

3. X. Shi1, A. Olvera, C. Hamilton, J. Li, L. Utke, **A. Petruska**, Z. Yu, **Y. Deng** and **H. Zhang**, "AI-enabled Robotic NDE for Structural Damage Assessment and Repair", July 2021

ME is mailed out to approximately **16,000 ASNT members each month**. Approximately half are US based and the rest are worldwide. Each paper is assigned a DOI number and added to the ASNT Library to be accessed by future researchers. Our last Technical Focus Issue was **open-access** and was accessed by approximately **12,000 readers**.

Figure 67. ME July 2021 special issue on robotic inspection.

Final video of the LTI robot in action is published on the youtube and can be accessed through the following link

https://www.youtube.com/watch?v=G5bEMXbZcJU

Workforce development

In this project, 5 undergraduate students, 4 master students, 3 Ph.D. students, and 1 postdoctoral scholar were involved. The PI and Co-PI of the project did an earnest attempt to promote diversity by including women and minority students.

Final remarks

The current project substantially contributed to science and technology by developing a first-of-a-kind robot to inspect tubular components. This project also contributed to workforce development by involving several students from diverse minorities.

The current LTI robot is at TRL level 4 and needs additional steps to get to a higher TRL level. The research team has been approached by several companies to use the technology indicating the huge gap and problem in inspection technologies that can be resolved by such a product. The commercialization of the product can be substantially enhanced if the TRL level gets to level 6 and above. The research team plans to submit a follow-up proposal to DOE's and other agencies' solicitations and programs such as STTR/SPIR to get additional support to increase the TRL level of the technology.

Acknowledgment: "This material is based upon work supported by the Department of Energy Award Number DE-FE0031649."

References

[1] H.D. Chattopadhyay, P., S. Ghoshal, A. Majumder, Locomotion Methods of Pipe Climbing Robots: A Review, J. Eng. Sci. Technol. Rev. 11 (2018) 154–165.

[2] C.J.L. Choi, S., H. Cho, Selection of Shear Horizontal Wave Transducers for Robotic Nondestructive Inspection in Harsh Environments, Sensors. 17 (2017).

[3] S. Choi, H. Cho, M.S. Lindsey, C.J. Lissenden, Electromagnetic acoustic transducers for robotic nondestructive inspection in harsh environments, Sensors (Switzerland). 18 (2018) 1–13. doi:10.3390/s18010193.

[4] H. Nemati, F. Alvidrez, A. Das, N. Masurkar, M. Rudraboina, H. Marvi, E. Dehghan-Niri, Integrating Electromagnetic Acoustic Transducers in a Modular Robotic Gripper for Inspecting Tubular Components, Mater. Eval. 79 (2021) 715–727. doi:10.32548/2021.me-04223.

[5] F. Xu, X. Wang, A Wheel-Based Cable Climbing Robot with Descending Speed Restriction, in: Chinese Control Decis. Conf., 2008: pp. 1570–1575.

[6] P.J. Shull, Nondestructive evaluation: theory, techniques, and applications, CRC press, 2016.

[7] M. Ghyabi, E. Dehghan-Niri, Comparison of coverage areas of two different sensor network arrangements for structural health monitoring of plate-like structures, in: Proc. SPIE - Int. Soc. Opt. Eng., 2019. doi:10.1117/12.2514402.

[8] E. Dehghan-Niri, S. Salamone, A multi-helical ultrasonic imaging approach for the structural health monitoring of cylindrical structures, Struct. Heal. Monit. (2014). doi:10.1177/1475921714548937.

[9] J.S.J. J.L. Rose, D. Jiao, Ultrasonic guided wave NDE for piping., Mater. Eval. 11 (1996) 1310–1313.

[10] S. Zamen, E. Dehghan-Niri, M. Ilami, V.A. Senthilkumar, H. Marvi, Recurrence analysis of friction based dry-couplant ultrasonic Lamb waves in plate-like structures, Ultrasonics. 120 (2022) 106635. doi:10.1016/j.ultras.2021.106635.

[11] M. Ghyabi, H. Nemati, E. Dehghan-Niri, A simplified framework for prediction of sensor network coverage in real-time structural health monitoring of plate-like structures, Struct. Heal. Monit. 21 (2022) 1379–1395. doi:10.1177/14759217211033217.

[12] H. Liu, X. Chen, J.E. Michaels, T.E. Michaels, C. He, Incremental scattering of the A0 Lamb wave mode from a notch emanating from a through-hole, Ultrasonics. 91 (2019) 220–230.

[13] T.E. Michaels, J.E. Michaels, Monitoring and characterizing corrosion in aluminum using Lamb waves and attached sensors, 6532 (2007) 1–11. doi:10.1117/12.715452.

[14] L. Yu, V. Giurgiutiu, In situ 2-D piezoelectric wafer active sensors arrays for guided wave damage detection, Ultrasonics. 48 (2008) 117–134. doi:10.1016/j.ultras.2007.10.008.

[15] X. Zhao, R.L. Royer, S.E. Owens, J.L. Rose, Ultrasonic Lamb wave tomography in structural health monitoring, Smart Mater. Struct. 20 (2011) 105002. doi:10.1088/0964-1726/20/10/105002.

[16] J. Krautkrämer, H. Krautkrämer, Ultrasonic testing of materials, Springer Science & Business Media, 2013.

[17] J.E. Michaels, T.E. Michaels, Guided wave signal processing and image fusion for in situ

damage localization in plates, Wave Motion. 44 (2007) 482–492. doi:10.1016/j.wavemoti.2007.02.008.
[18] J.W. Tukey, Exploratory data analysis: past, present and future., Princeton, NJ: PRINCETON UNIV NJ DEPT OF STATISTICS., 1993.
[19] Hintze, Jerry L., R.D. Nelson, Violin plots: a box plot-density trace synergism, Am. Stat. (1998) 181-184.
[20] and M.I. H. Marvi, E. Dehghan-Niri, Systems and methods for a Lizard-Inspired Tube Inspector (LTI) robot, US 2020/0324415A1, 2020.